Designing an Experiment to Investigate Slow Light Effects in Whispering Gallery Mode Resonators

Karolina Disa Dorozynska
Supervisors: Andreas Walther,
Stefan Kröll

Master's Thesis
VT 2015

LUND
UNIVERSITY

Department of Physics
Atomic Physics Division

Abstract

Slow light and Whispering Gallery Mode Resonators are two interesting and useful fields with applications in optical sensing and laser stabilisation among others. Slow light can lead to long interaction times which are useful in light-matter interactions such as sensitive non-linear optics. Whispering Gallery Mode Resonators have small mode volumes and strong beam confinement leading to high Quality Factors and intense trapped light. Whispering Gallery Mode Resonators exhibit very narrow resonance linewidths which are beneficial in frequency sensitive measurements.
This thesis uses a Praseodymium REI doped Yttrium orthosilicate crystal, formed into a disc shaped Whispering Gallery Mode Resonator. The aim is to design a setup which can be used to combine the two fields, slow light and Whispering Gallery Mode Resonators, in an attempt to achieve ultra-high Quality Factors and ultra-narrow resonance linewidths. The thesis details the experimental mode coupling procedure learnt from a group at Max Planck Institute for the Science of Light in Erlangen, Germany. The thesis provides a foundation for Whispering Gallery Mode Resonator experimentation in the Quantum Information group in Lund, where the thesis work was undertaken. The resulting knowledge gained is applied to design a setup holder for use in a cryostat, which provides the necessary temperatures to create slow light structures. Two beam alignment setups are constructed and used to couple into the Whispering Gallery Mode Resonator at room temperature. The first of the two setups (free beam) was difficult to operate and control over the beam alignment and focal spot shape was poor. The resulting mode coupling had a low efficiency. The second setup (fibre coupled) provided a more user friendly setup with good control over the beam alignment and focal spot shape. Results using this setup were taken for a variety of wavelengths between 593.1 nm and 610.4 nm to investigate the effect of the ions wavelength dependent absorbance, on the losses. Due to the low efficiency of the coupling in both regimes it was not possible to isolate the cause. A mismatch of focal spot size and shape is suggested as a potential area that introduces loss and therefore requires more extensive investigation. With improved beam alignment, in addition to the focal spot geometry, it should be possible to perform the absorbance measurements again in order to determine the contribution. Suggestions for further measurements including the surface roughness and mode simulations are made in an attempt to optimise the mode coupling regime to be able to accurately estimate the Quality Factor of the Whispering Gallery Mode Resonator. This is critical in order to observe changes in the Quality Factor value at cryogenic temperatures, which can be attributed to slow light effects alone.

Acknowledgements

Firstly I would like to thank my supervisor Andreas Walther for his helpful explanations when things were unclear. I would also like to thank my assistant supervisor, Stefan Kröll and head of the Quantum Information group in Lund for giving me the opportunity to undertake this thesis research. I would also like to thank the entire Quantum Information group for making me feel welcome from day one and providing a very friendly and warm working environment. Lars, for his probing questions which made me think about the physics that extra bit. Jenny, for her constant optimism and friendship. Adam for his help in all things laboratory based and of course those I shared an office with, Diana, Qian, Yupan and Sofia.

Thanks must also go to Harald Schwefel and his group at the Max Planck Institute for the Science of Light in Erlangen, Germany. Not only did they fabricate the Whispering Gallery Mode Resonator used in this thesis work but they also welcomed me into their group for 2 weeks to learn about Whispering Gallery Mode Theory and experimental coupling. Special thanks to Richard, Martin, Florian and Alfredo, all of whom also instructed me on the theory and experimental techniques as well as being great company.

I would also like to thank Håkan Ivansson for making the holder used for the experiments and Jason Beech for providing wax, a laboratory and his time so that I could attach the prism to the baseplate. I would also like to thank the people in the Atomic Physics division who have made the environment welcoming from the start and a pleasure to work in.

Finally, but not least importantly I would like to thank my friends Panagiota and Alexis for their unending friendship. I would like to thank my parents Monica and Stan for their support, making it possible to undertake my masters in Lund. I would also like to thank my partner and best friend Kenneth, who has been there every step of the way.

Contents

Abbreviations

ECDL- External Cavity Diode Laser

EM- Electromagnetic

FP- Fabry-Perot

FSR- Free Spectral Range

FTIR- Frustrated Total Internal Reflection

HeNe- Helium-Neon

MPL- Max Planck Institute for the Science of Light, Erlangen, Germany.

PBS- Polarising Beam Splitter

Q-Factor- Quality Factor

QI- Quantum Information

REI- Rare-Earth-Ion

SHB- Spectral Hole Burning

SML- Single Mode Fibre

TIR- Total Internal Reflection

WGM- Whispering Gallery Mode

WGMs- Whispering Gallery Modes

WGMR- Whispering Gallery Mode Resonator

WGMRs- Whispering Gallery Mode Resonators

YSO- Yttrium Orthosilicate

1 Introduction

Since the development of the laser in the 1960s many areas of research have benefited from its unique properties of monochromaticism, directionality and coherence. Many new technologies have been developed which incorporate lasers as well as many new discoveries due to the use of lasers in research. The two areas discussed in this thesis and described below; i) Slow Light and ii) Whispering Gallery Mode Resonators (WGMRs), have been made possible through the invention of the laser. Slow light effects, resulting from the generation of slow light structures as well as WGMRs, rely on the unique beam properties that lasers provide. Both of these topics have beneficial properties of their own which have uses in a number of different applications such as increased frequency sensitivity. If the two topics could be combined it may be possible to enhance the characteristic properties of both.

Electromagnetic (EM) waves are described by the phase (the individual sinusoidal components of the wave) and the group (envelope of the wave resulting from all the phase components) velocities. The phase velocity is defined by the refractive index of the medium through which the EM wave propagates. If the refractive index of a medium is constant then the group and phase velocities are the same. If the refractive index experienced by the EM wave, however, varies then the medium is known as dispersive, since the EM wave becomes dispersed due to varying wavelength dependant velocities. If the change in the refractive index experienced is rapid and positive, then the group velocity will be significantly reduced, leading to slow light.

Slow light is defined as being several orders of magnitude smaller than the speed of light in a vacuum, c. This great reduction in speed has been achieved in a variety of different ways such as Electromagnetically Induced Transparency and Spectral Hole Burning (SHB) and has lead to benefits in a variety of areas. Due to the longer propagation time of the light there can be a longer interaction time between the light and atoms. This means exceptionally sensitive non-linear optics experiments can be performed without needing to use very high intensity lasers, which is currently required [1]. Another application of slow light, due to the increased frequency resolution, is in the development of more frequency sensitive interferometers, ultimately leading to improved optical sensing devices [8].

WGMRs are specially shaped cavities which can be spherical, toroid or disc shaped, to name a few. They, unlike conventional mirror cavities, rely on containing light within them by total internal reflection. This results in low loss and high intensity, confined light. WGMRs therefore have high Quality Factors (Q-Factors), defined as the inverse of the loss. WGMRs also have very narrow resonance linewidths making them very useful for frequency sensitive applications. Due to the characteristic properties of the WGMRs, high Q-Factor, small mode volume and high intensity confinement they have also found use in enhancing the spontaneous emission of ions in resonant cavities, where the enhancement is known as the Purcell factor [3], [4] .

This thesis aims to provide the foundation for an experiment to investigate slow light effects in WGMRs. This experiment combines the field of slow light with the field of WGMRs to see if the beneficial properties which they exhibit could be enhanced when used in conjunction. The thesis combines existing knowledge of creating slow light structures, which are used in the quantum memory research at Lund University, with a Rare-

Earth-Ion (REI) doped WGMR. If it is possible to achieve record high Q-factors and ultra-narrow resonance linewidths, the QI group at Lund could benefit not only from the increased knowledge in the combined fields but also from the application in, for example, laser stabilisation. The latter is achieved by optical feedback where the WGMR would provide a more precise frequency as a reference due to the decreased linewidth.

1.1 Aim of the Thesis

Spectral Hole Burning (SHB) relies on targeting a spectrally selective material with a narrow frequency laser in order to create a transmission window in the materials absorption profile. When a narrow transmission window is created a sharp and positive change in the refractive index results. This feature is known as a slow light structure since when a light pulse passes over it, its group velocity will be significantly slowed down. This 'slow light' therefore takes a longer time to propagate which could result in changes to the Q-factor of resonators, due to increased photon lifetime.

WGMRs are a family of resonators which have been found to have high Q-Factors, that is to say that they have low optical loss since the Q-Factor is a measure of the inverse loss per optical cycle. A cavity can have a number of different loss mechanisms which, when all considered together, give the total resonator loss. When coupling to WGMRs it is possible to measure the Q-Factor by studying the linewidth of the mode or modes coupled to. The Q-Factor is related to the linewidth by $Q = \frac{\nu}{\delta\nu}$ where ν is the resonant frequency and $\delta\nu$ is the linewidth, in Hertz. Subsequently it becomes clear to see that as the linewidth increases, the value of the Q-Factor decreases. The linewidth depends on the losses; therefore, if the cavity losses can be reduced, it is possible to achieve a more narrow resonance linewidth. It is also possible to express the Q-Factor in terms of the photon lifetime, τ , using the following expression; $Q = \omega\tau$, with ω being the angular frequency. It is therefore possible to increase the Q-Factor by extending the time the photon spends in the cavity.

This thesis presents the preliminary investigation and experimental design in order to pursue an investigation into slow light effects in WGMRs. Since the slow light structures created from SHB can lead to increased photon lifetime in a cavity it is interesting to see whether it is possible to achieve record narrow resonance linewidths. Consequently it is therefore perhaps possible to achieve a record high Q-Factor. The thesis aims to design a setup which can be used to perform SHB in a WGMR. The thesis presents theory on both topics and experimental mode coupling performed at room temperature. The techniques used and the results obtained provide the information and experience required to perfect the final experiment. The thesis also aims to act as a reference for future use in the QI group in Lund, since WGMRs have not been studied or used in it before. The thesis therefore includes details needed for others who will follow, especially with consideration on how to experimentally couple to a WGMR. Due to the absence of WGMR research in the QI group, collaboration with a group at the Max Planck Institute for the Science of Light in Erlangen, Germany (MPL), who have extensive experience in the field of WGMRs research, was undertaken. Chapter 3 describes the experimental

coupling procedure as performed at MPL in great detail so that it should be possible for readers of the thesis to replicate it.

1.2 Outline of the Thesis

This thesis is divided into 8 chapters. Chapter 2 presents the theory of REI doped crystals and the manipulation of their absorption profiles to generate slow light features. It continues onto explaining the theory of WGMRs including mode structure and volume, determining the Q-Factor and how to achieve coupling into the modes. Chapter 3 then presents the experimental procedure to mode couple into WGMRs from initial experimental work done at MPL. How to characterise the WGMR, such as experimentally determining the Free-Spectral Range (FSR), the Q-Factor and coupling efficiency are also presented in this chapter. Since the thesis aims to combine SHB and WGMRs, the use of a cryostat will be required, as is explained in chapter 2. Chapter 4 therefore outlines the requirements for performing mode coupling, followed by eventual SHB, within a cryostat. The experimental geometry and individual components of the coupling setup are discussed, culminating in the proposed design of a holder able to fulfil the necessary requirements. Chapter 5 gives an overview of the two different experimental setups used to couple light into the WGMR. Chapter 6 presents the results from the two methods used for coupling into the WGMR and problems encountered with their operation. All the results are taken at room temperature and form a preliminary investigation into creating a suitable setup for the future experiment. Chapter 7 provides a conclusion of the main points that can be drawn from this project and an outlook for future considerations.

2 Background

This section provides the theory required to follow the main text of this thesis. It is divided into two main sections; firstly covering the REI doped crystal and its properties and manipulation of them; secondly, WGMRs are introduced and some of their key properties are discussed in further detail. Although SHB is not performed as a part of this thesis, the aim of it is to provide the foundation for investigating slow light effects in WGMRs. Since SHB leads to the creation of slow light structures it is a necessary area of theory to cover in order to gain a clear overview of this work and of experiments that will stem directly from it. The chapter begins with details of the properties of the doped crystal used to fabricate the WGMR and presenting information about the energy level structure of the dopant. It then continues to explain how the dopant can be optically manipulated in order to create holes in the absorption profile, which ultimately lead to structures which cause the group velocity of a passing light pulse to be slowed down. The second section is devoted to WGMR theory starting with the method of light confinement in them and followed by key features and properties of them which are useful to know and are also used in later chapters of the thesis.

2.1 Creating Slow Light Structures

Light travelling in a vacuum is undisturbed by the presence of matter [1]. When light propagates through matter, however, it experiences a reduction in speed. This is because a change in the phase velocity of the light occurs. The refractive index, n, of a medium describes the ratio between the speed of light in a vacuum, c, and the phase velocity of the light in that particular medium. The refractive index of a medium can vary depending on the frequency of the light propagating through it, resulting in different phase velocities for different frequencies, an effect known as dispersion. Media which exhibit this property are known as dispersive. Dispersive media can also impact the group velocity of a wave since it is dependent on how the refractive index changes with respect to the frequency. It is also possible to slow the group velocity of light if it experiences a region with a rapid and positive change in the index of refraction. When this occurs it is called 'slow light'. The following sub-chapter gives the reader a background of the doped crystal used for the WGMR and leads onto the process of SHB. It culminates in a brief conclusion of how the result of SHB creates structures which lead to the above described, 'slow light'.

2.1.1 Praseodymium Rare-Earth-Doped Crystal

This thesis uses a Praseodymium REI doped Yttrium orthosilicate ($Pr^{3+} : Y_2SiO_5$) crystal, also known as Pr:YSO. It is the embedded REIs which are targeted and manipulated. The ions are used due to their favourable properties, e.g. their long excited state coherence time. It should be noted, however, that these properties can only be achieved at liquid helium temperatures, i.e. <4K since decoherence mechanisms are strongly effected by crystal lattice phonon effects above these temperatures. For this reason it is necessary

[1] However there can be exceptions to this statement, e.g. in the case of gravitational lensing.

for the doped crystal to be contained within a cryostat for experiments.

The REI, praseodymium, exhibits hyperfine electronic state splitting. The size of the hyperfine splitting is additionally effected by the crystal in which the ions are embedded via the Stark effect. There is also ion-ion interaction via the second-order hyperfine and quadrupole interaction which lead to additional distortions in the hyperfine energy level separations [2].

Figure 1 illustrates the hyperfine energy level splitting of the transition $^3H_4$ to $^1D_2$ for $Pr^{3+} : Y_2SiO_5$, the crystal from which the WGMR is fabricated. The lower three levels are the ground states and the upper three are the excited states. Between all of the 6 hyperfine energy levels there are a total of 9 possible transitions. Each of these transitions has its own probability for absorption or transmission, known as the oscillator strength, and these values are given in figure 1(b).

The crystal structure leads to the ions ending up in two possible sites known as site 1 and site 2. Site 1 has the wavelength of 605.813 nm whereas site 2 has the wavelength of 607.770 nm. The majority of the ions are located in site 1 (circa 90%) and therefore all the experiments will be performed around 605.813 nm, excluding the initial coupling process discussed in chapter 3, from which no formal results were taken. The host crystal, YSO, is optically transparent around this wavelength.

a

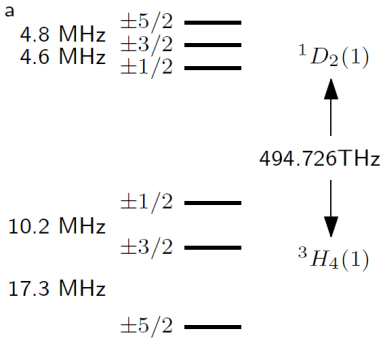

b

g \ e	±1/2	±3/2	±5/2
±1/2	0.56	0.38	0.06
±3/2	0.39	0.60	0.01
±5/2	0.05	0.02	0.93

Figure 1: (a) Diagram of the hyperfine energy levels of praseodymium, where the three lower levels are ground levels and the three upper levels are the excited levels. (b) a table of the oscillator strengths of the praseodymium ions for the 9 possible transitions between its hyperfine levels. The figures are taken from the PhD thesis by L.Rippe.[5]

2.1.2 3-Level System

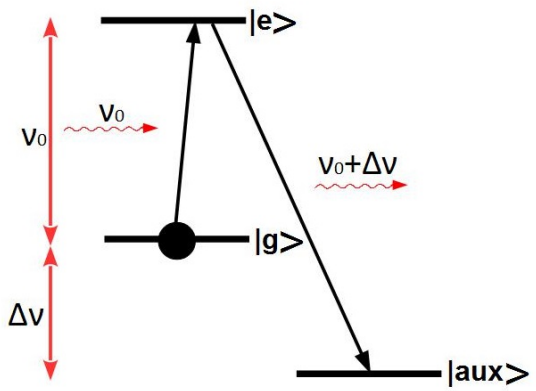

Figure 2: An illustration of the 3-level system of a praseodymium ion. $\mid g >$ represents the hyperfine ground level being cleared by a driving laser frequency ν_0. $\mid e >$ represents one of the upper three excited levels which lies ν_0 away from $\mid g >$. $\mid aux >$ collectively describes the remaining hyperfine ground levels of the ion.

Here a more generalised view of the ion transitions is considered using a three level system, as indicated in figure 2, instead of six as described previously. This simplification is presented since when considering SHB, one transition is driven by a laser frequency equivalent to ν_0. The de-excitation occurs according to the oscillator strengths presented in figure 1 (b), to all the hyperfine ground states. To achieve SHB the driven transition is cleared and so for simplification the 3-level system shows the de-excitation from $\mid e >$ to $\mid aux >$, which describes the remainder of the hyperfine ground levels. Figure 2 illustrates a hyperfine ground level , $\mid g >$, an auxiliary level, $\mid aux >$, which collectively describes the other hyperfine ground states and an excited state, $\mid e >$, which can be any one of the upper hyperfine levels. It is possible for the atom in the hyperfine ground state $\mid g >$ to absorb a photon with an optical frequency equal to ν_0 and be excited up to the excited state $\mid e >$. Subsequently it can decay from $\mid e >$ to either of the lower levels $\mid g >$ or $\mid aux >$ by two different methods, spontaneous or stimulated emission. When the state decays it emits a photon with a frequency that corresponds to the transition [7]. Due to the lifetime, T, of the excited state, which is the time it takes for spontaneous emission to occur, homogeneous broadening occurs in the transition spectrum [7]. This gives a transition line width known as the homogeneous line width, Γ_h, which is described by equation (1). From this relationship it can clearly be seen that if the lifetime is long then a narrow line width will result.

Homogeneous linewidth:

$$\Gamma_n = \frac{1}{\pi T} \tag{1}$$

where T is the lifetime of excited state. (for spontaneous emission to occur).

2.1.3 Inhomogeneous Broadening

We now have an understanding of the light-matter interaction undergone when considering one of the Pr^{3+} ions in the crystal. Let us now consider multiple embedded ions to gain a picture of the entire crystal. The ions are distributed throughout the host crystal, which is in turn illuminated by laser light corresponding to the transition between $\mid g >$ and $\mid e >$.

If all the ions have the same transition frequency, a single line width, Γ_h, will describe all of the ions transitions. In reality no crystal is perfect and the ions embedded within it are not regularly, but randomly, distributed throughout it. As a result, each of the ions will experience a different local environment. The numerous local environments distort the energy level separations of the ions leading to a range of different transition lines. All the ions in the crystal are therefore collectively described by several homogeneous line widths which leads to a broadened line shape known as the inhomogeneously broadened line width, Γ_{inh}.

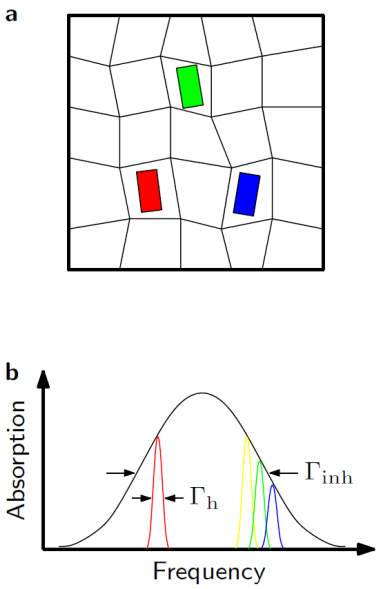

Figure 3: (a) Illustrates the embedded ions, coloured green, red and blue, embedded in a crystal host. The uneven boxes indicate the distortions which occur leading to different energy level transitions. (b) Illustrates the homogeneous linewidths of the ions, in red, yellow, green and blue. The black curve represents the shape of the in-homogeneously broadened linewidth due to the spread of homogeneous linewidths of the ions. The figures are taken from the PhD thesis by L.Rippe.[5]

The homogeneous line widths are normally a few Hz, however, by comparison the inhomogeneous line width is in the GHz range, [7]. Figure 3(a) illustrates the ions in the crystal host where the distortions of the grid represent distortions of the local environments. Each ion, with a differing homogeneous line width, is represented by a different colour. In figure 3(b) the corresponding homogeneous line widths of the example ions can be seen and lie under the inhomogeneously broadened line width which describes the full frequency range of the ions transitions.

2.1.4 Spectral Hole Burning

Since the inhomogeneous line width envelopes a range of narrow homogeneous line widths the result is a spectrally selective material. This means that it is possible to use a narrow line width laser to excite only a small selection of ions in the material if their frequencies match. It is due to the spectral selectivity of the inhomogeneous line width that it is possible to perform SHB.

Consider the ions whose transition from $\mid e >$ to $\mid g >$ is equivalent to a frequency ν_0. If these ions are illuminated by a laser with frequency ν_0, they will become excited. Once in the excited state they can spontaneously decay to one of the available hyperfine ground state levels by a particular probability, presented previously in figure 1(b). Let us assume for the sake of explanation that the decay of the excited electron is on the transition $\mid e >$ to $\mid aux >$. The electrons in the $\mid aux >$ state can no longer be excited back up to the $\mid e >$ level since the laser frequency does not match the $\mid aux >$ to $\mid e >$ transition.

When all the ions in level $\mid g >$ have been excited to $\mid e >$ and subsequently decayed to $\mid aux >$ there are no longer any electrons available to absorb the photons from the laser beam. This lead to a transmission window at the frequency ν_0 which, when viewed as part of the absorption spectrum of the material, is seen as a hole since no absorption can occur there any more.

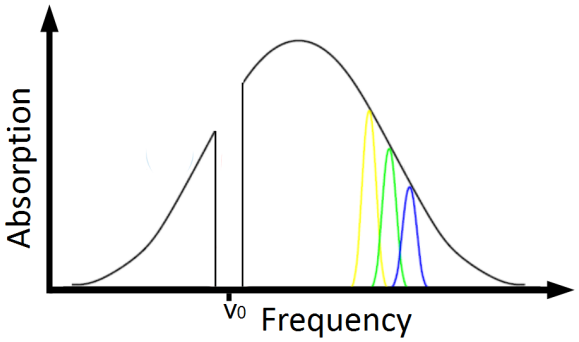

Figure 4: A sketch of the in-homogeneously broadened linewidth of praseodymium ions with a spectral hole at frequency, ν_0. A transmission window has been created in the absorption profile due to pumping of the transition equivalent to ν_0, by a laser. The figure is adapted from one in the PhD thesis by L.Rippe. [5]

2.1.5 Slow Light

A spectral hole is an example of a slow light structure, a structure which modifies the group velocity of a pulse such that it is greatly slowed down. Figure 5 illustrates a pulse of light, where the phase, ν_p and group, ν_g velocities are marked. Slow light is defined as light whose group velocity is much slower than that of the velocity of light in a vacuum, c.

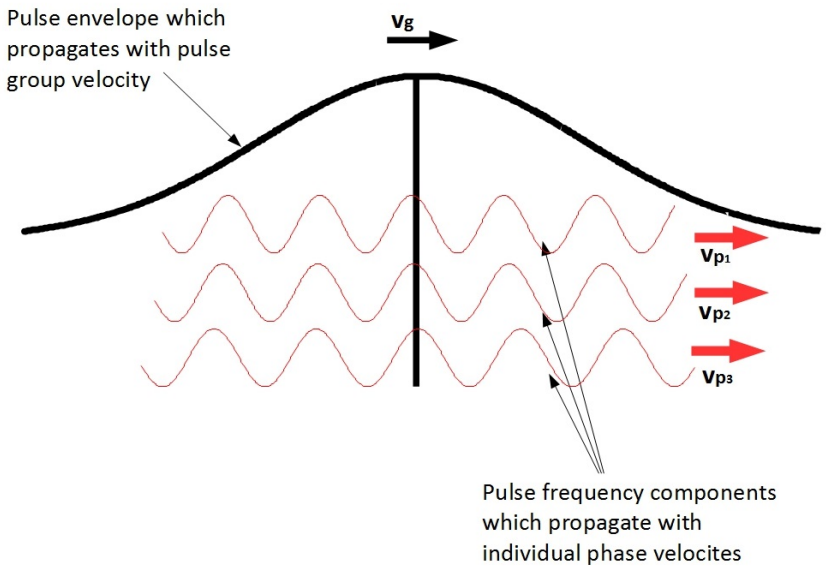

Figure 5: A sketch of the phase, ν_{p1}, ν_{p2}, ν_p, and group velocities, ν_g of a pulse of light.

When a spectral hole is created which exhibits a region outside it where the absorption is very high e.g. $\alpha L = 80$ and inside it is close to zero, a strong dispersion results [6]. The change in the absorption over the narrow spectral range, due to the hole creation, brings about a change in the refractive index over the narrow region. If the refractive index change is rapid and positive it leads to an extremely low pulse group velocity, i.e. Slow Light. This is the case for narrow holes created in SHB. Figure 6 illustrates how the index of refraction varies over a narrow spectral hole.

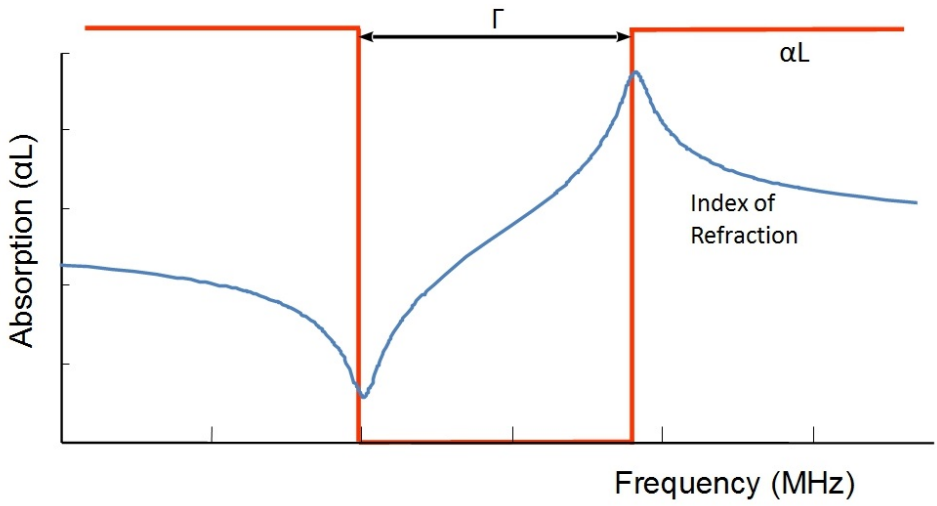

Figure 6: A sketch of the change in refractive index over a narrow spectral hole, resulting from spectral hole burning.

$$n_g = n_p + \omega \frac{dn_p}{d\omega} \tag{2}$$

$$\Delta = \frac{n_g L}{c} \tag{3}$$

The relationship between the change in refractive index and group velocity index is given by equation (2) where n_g is the group index, n_p is the phase index and ω is the angular frequency. A small group index corresponds to slow light. The derivative of the group index gives a large contribution to n_g since the slope is steep. This arises due to the hole creation being over a narrow spectral region. Additionally equation (3) is given which describes the relationship between the group index and the time delay of the light pulse, [8].

2.2 Evanescent Waves

Evanescent waves are used to achieve mode coupling in the experimental portions of this thesis work. Here a brief introduction to some of their properties and how they arise are given.

Snell's Law:

$$n_1 sin\theta_1 = n_2 sin\theta_2 \tag{4}$$

First we should consider TIR which can be described using Snell's Law. Typically this law is used when considering refraction of a beam which occurs at the boundary of two media with differing refractive indices, n_1 and n_2. If the beam propagates though the first medium, n_1, where $n_1 > n_2$, it will be deflected away from the normal to the boundary upon entering the second medium, n_2. Of course this is not true for all angles of the incident beam. Figure 7(a) shows how the refracted angle, θ_r, varies with respect to the incident angle, θ_i. For each of these angles, θ_i, the refracted beam continues propagation through the second medium, however at a certain angle, θ_C, known as the critical angle, this is no longer the case.

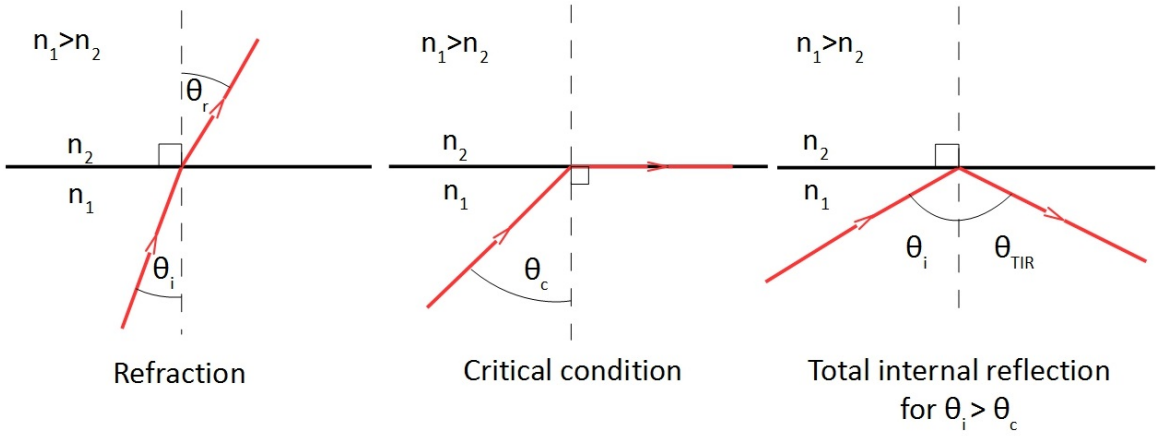

Figure 7: from left to right; (a),(b) and (c). (a) an illustration of refraction of a beam from a high to low refractive index. (b) an illustration of the critical condition as defined by Snell's Law. (c) illustrates total internal reflection at a boundary from a high to low refractive index. The beam is reflected back into the first medium at the same angle it was incident with.

Figure 7(b) illustrates the critical condition. Figure 7(c) illustrates that for angles greater than θ_c, TIR occurs. Although the beam is now reflected and no longer refracted along a path within the second medium, waves are still present in the second medium. These are known as evanescent waves, [9]

Critical Condition:

$$\theta_c = sin^{-1}\left(\frac{n_1}{n_2}\right) \tag{5}$$

Using electromagnetic wave formalism it is possible to more precisely describe the nature of evanescent waves. Since no detailed mathematics of the evanescent field is done as a part of this thesis, however, only some details of it will be discussed here. The reader is welcome to find a more in depth description of evanescent waves in the book by F. de Fornel, [9]. Figure 8 shows how the electric field of the evanescent waves in the second medium decays exponentially.

From this decay profile it is possible to extract the penetration depth of the evanescent field which, as per figure 8, is the distance at which the electric field at the boundary, E_0, is divided by e.

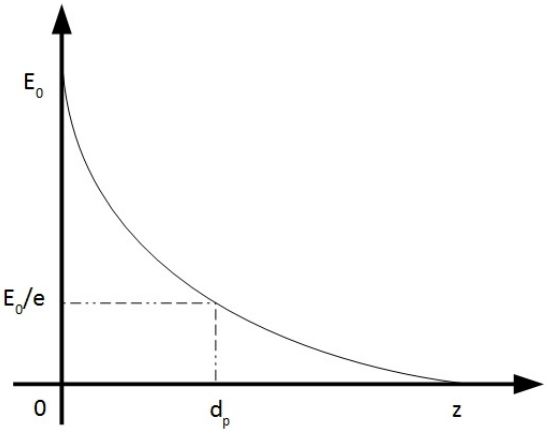

Figure 8: A sketch of the exponentially decaying evanescent field as a function of distance, z (perpendicular to the boundary from where TIR occured).[9]

Penetration Depth of Evanescent Field:

$$d_p = \frac{\lambda}{2\pi\sqrt{n_1^2 sin^2\theta - n_2^2}} \tag{6}$$

where; θ is the angle in the prism leading to TIR, n_1 is the refractive index of the first medium, n_2 is the refractive index of the second medium and λ is the wavelength of the incident beam.

The evanescent field transports an average energy equal to zero. It is therefore not possible to detect evanescent waves directly. If the system from which the evanescent field is perturbed then the evanescent wave value, at a particular point, can be determined. This occurs as a result of the transformation of the evanescent wave into a propagative one. This process is known as frustrated total internal reflection (FTIR) and it forms the basis of evanescent coupling into WGMRs, as will be discussed in more detail later.

2.3 Whispering Gallery Mode Resonators

An optical cavity, or resonator, is a device which confines light and allows particular frequencies to resonate. An optical cavity normally consists of at least two, sometimes

more, mirrors off which light is reflected and contained within a closed loop path. The optical path length of the enclosed light depends on the cavity geometry. If it is an integer multiple of the wavelength of the light confined then constructive interference can occur. This results in a preferential build up, or resonance, of that particular frequency and this is known as the resonance condition.

The Fabry-Perot (FP) resonator is an example of an optical cavity and consists of two planar mirrors in-between which light is reflected, experiencing some loss in each round trip. Light which is coupled into the FP resonator is largely reflected off the first mirror, limiting the amount of light that can be trapped inside the cavity. Instead of mirrors it is possible to use dielectric materials, where the light is totally internally reflected at the boundary between it and the surrounding medium provided the dielectric has the higher refractive index. A Whispering Gallery Mode Resonator (WGMR) is an example of the latter, where light is confined along the inner edge due to the curvature of the cavity. Light can be coupled into WGMRs by means of an evanescent field which results in greater light confinement since the incident light is not reflected off the surface. WGMRs therefore have higher light intensities compared to FP resonators. WGMRs exist in several geometries such as spherical, microtoroidal and disk.

Whispering Gallery Modes where first explained in acoustic waves, by Lord Rayleigh, from his observations at St.Pauls Cathedral Whispering Gallery in London, circa 1910 [11]. It was not until 1961 ,[10], however, that Whispering Gallery Modes (WGMs) where observed in optics. Since the confined light is directed by total internal reflection (TIR) it experiences much lower loss than reflection off mirrors in conventional cavities. As a result WGMRs have very high Q-factors, in the region of 10^{11}, [12] compared with a Fabry-Perot cavity with Q-factor 5.6×10^5, [13] This also means that WGMRs have narrow resonance linewidths, high light energy and long photon lifetime. This has lead to their use in frequency stabilisation, sensing and optical filters, to name a few.

This chapter seeks to define the characteristics of WGMR modes as well as explaining the coupling procedure theoretically. Experimental coupling and characterisation methods will be discussed in chapter 3.

2.3.1 Whispering Gallery Modes

We will begin by considering WGMs using the ray optics formalism. Snell's law has previously been mentioned along with the critical condition required before TIR can occur. The WGMR is a specially shaped dielectric resonator. If we consider a ray incident on the boundary of a dielectric, from within it, at an angle $> \theta_c$ then the ray will be totally internally reflected. Figure 9 shows a two-dimensional sketch of a circular cavity with a confined light ray.

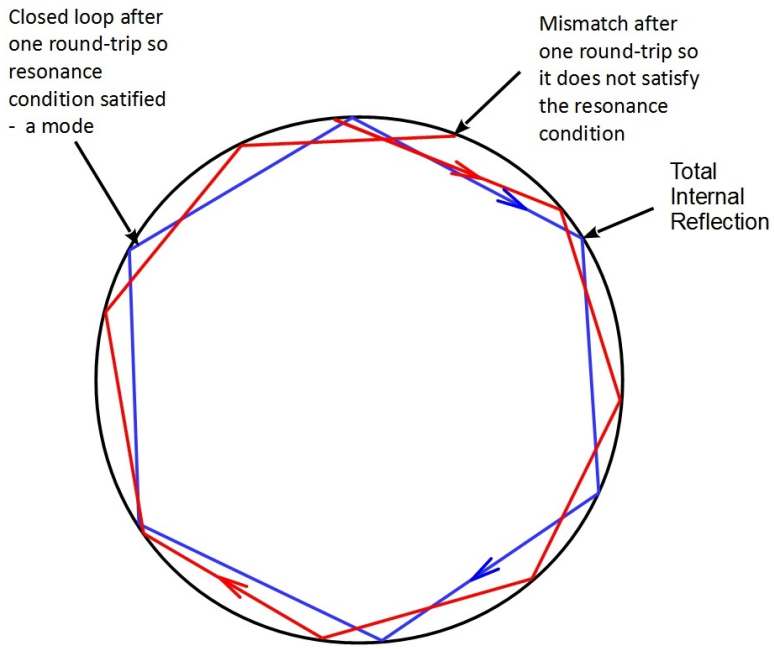

Figure 9: Mode structure in a Whispering Gallery Mode Resonator using the ray optics formalism. The blue line illustrates a beam whose optical path after one round trip, creates a closed loop and is therefore able to resonate in the cavity. This is a supported mode. The red line illustrates a beam which does not form a closed loop path and therefore does not resonate in the cavity. This is not a supported mode.

The light ray meets the cavity edge at an angle $> \theta_c$ causing it to be TIR but due to the circular shape of the cavity a small portion of the wave can leak out. This will be considered in more detail in section 2.3.4. The circular shape also means that the ray repeatedly meets the edge at the same angle, $> \theta_c$, and is therefore contained within the cavity. This means that the ray is guided along the circumference experiencing N_R reflections until it overlaps with its original starting position. Depending on the frequency of the light, if after a round-trip the ray is in phase again a standing wave resonance will occur. This is what is known as a Whispering Gallery Mode, [11].

For low order, fundamental, modes it is possible to use an approximation for the resonance condition. This is because if N_R is sufficiently large it can be assumed that the round trip path of the light ray is close to the circumference of the circle, [11].

2.3.2 Mode Structure

The ray optics description allows a basic and more intuitive understanding of WGMs. WGMs do not just exist confined along the inner rim of WGMRs, however, but higher order WGMs are found further inside the resonator. To gain a full understanding of WGM structure it is necessary to turn to the EM wave description. However since it will not be delved into in any great detail the reader is able to find a more extensive description in the Review by Harald Schwefel [14].

In WGMRs there are three dimensions to consider, the radial, the polar and azimuthal. Figure 10 shows the directions in which the modes are defined as well as examples of the mode structure through a slice of the WGMR. Note that the polar (or axial) radius of curvature is defined as ρ in the figure however throughout this thesis, r, is used instead.

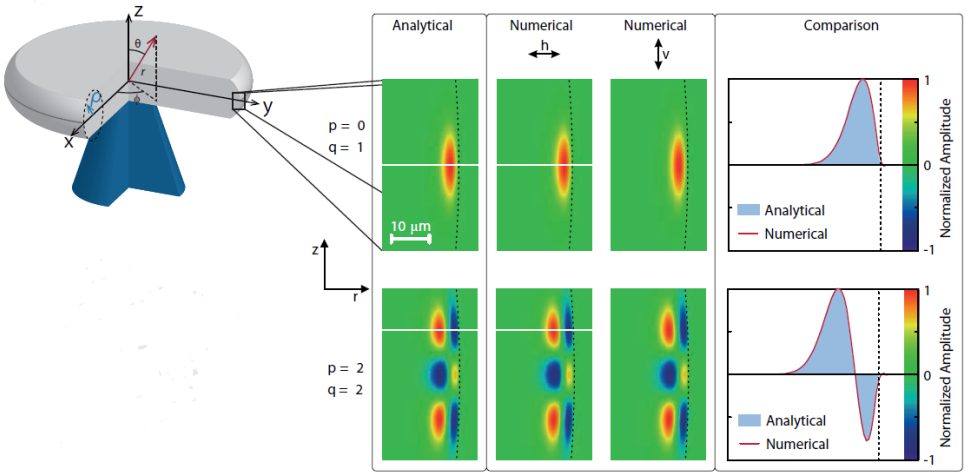

Figure 10: Schematic of the mode structure using the electromagnetic wave formalism. The spherical coordinate system in the Whispering Gallery Mode Resonator is illustrated on the left and on the right the electromagnetic field distribution is shown for some example values of the mode numbers defined as m,p and q. m is the number of wavelengths around the WGMR equator, p is the number of nodes in the polar direction and q is an integer solution of the spherical Bessel functions. The mode number notation in the main body of the thesis does not match the letters used in this figure but they are equivalent.[14]

WGMs are described using three parameters, l, m and q, which are used for the polar, azimuthal and radial modes respectively. $2l$ gives the number of maxima in the azimuthal direction and to calculate the number of maxima in the polar direction one uses l-m+1. The mode number q defines the maxima in the radial direction. From the above parameter relationships it is possible to see that the fundamental mode is described as q=1 and l=m, where l and m are very large numbers. Modes with q >1 exist deeper within the WGMRs.

2.3.3 Mode Volume

Here the mode volume is presented since it will be used to estimate the spot size of the fundamental mode of the WGMR. WGMRs exhibit small mode volumes and long confinement times and as a result, high intensities can be achieved in them. It is possible to determine the mode intensities by calculating the approximate mode volume given by equation (7). It should be noted that this equation has been derived for a spherical WGMR type, however, the WGMR used in this thesis is disk shaped. The thickness of the disk is therefore a limiting factor when considering the mode volume using this

approximation.

$$V_{eff} = 3.4\pi^{\frac{3}{2}} \left(\frac{\lambda}{2\pi n}\right)^3 l^{\frac{11}{6}} \sqrt{l - m + 1} \tag{7}$$

where V_{eff} is the effective mode volume, λ is the wavelength, n is the refractive index, and m and l are the previously defined mode numbers, [11].

$$l = \frac{\pi n d}{\lambda} \tag{8}$$

If the resonator size is large compared to the wavelength then the l number can be estimated using equation (8).

2.3.4 Quality Factor

$$Q = \frac{StoredPower}{PowerLoss} \tag{9}$$

There are several mechanisms contributing to the total loss in WGMRs. Depending on the material chosen for the WGMR, the geometry or the coupling technique, certain mechanisms can dominate over others. The Q-Factor is often used to give an indication of the loss of a WGMR since it is defined as the ration between the stored energy and the lost energy, as described by equation (9).

$$Q = \frac{2Fl}{\lambda} \tag{10}$$

where; F = finesse, λ = wavelength and L = length of resonator (approximated circumference).

$$F = \frac{FSR}{\Delta\lambda} \tag{11}$$

$$Q = \frac{\lambda_0}{\Delta\lambda} = \frac{\nu_0}{\Delta\nu} \tag{12}$$

where; λ_0 = wavelength of a resonance, $\Delta\lambda$ = is the resonance linewidth, ν_0 and $\Delta\nu$ are the same but in terms of optical frequency.

It can be calculated in several different ways as shown in equations (10), (12) and (13). Equation (10) uses the Finesse, defined in equation (11), which therefore relates the Q-factor to the free spectral range (FSR) and the resonance linewidth, $\Delta\lambda$. The Q-factor, FSR and resonance linewidth are important terms in the characterisation of WGMRs.

Due to the nature of the results obtained experimentally it is easier to determine the Q-factor using the relation given in equation (12). This is because it is possible to measure the resonance frequency and its full width half maximum (FWHM) linewidth quite simply. It is this method which is used to experimentally determine the Q-factor throughout this thesis.

$$Q = \omega \frac{E_{stored}}{P_{loss}} = \frac{2\pi\nu_0 T_{rt}}{I} \tag{13}$$

where; P_{loss} = power lost per cycle, ω = angular frequency, ν_0 = optical frequency, E_{stored} = energy stored per cycle, T_{rt} = round trip time in cavity and I = relative power loss in each round trip.

Equation (13) gives an alternative perspective on how the Q-factor can be determined. If we focus on one feature of the equation alone it is possible to draw some conclusions about how the Q-factor can be varied. The round trip time in the cavity is straightforward in that it considers the confinement of the photon in the cavity. The fundamental modes are those with the highest Q-factor and that can be seen directly from equation (13). The fundamental modes travel more or less along the circumference of the resonator and therefore have the longest optical path lengths. This obviously means that they spend more time in the cavity than other modes, if they all propagate with the same speed. If we now consider the photon confinement, not by path length, but by speed of the propagating light it is possible to see how slow light effects can result in an increased Q-factor, and in turn lead to a narrowed resonance linewidth. If we consider that a slow light structure has been created and that a light pulse has passed over it resulting in a reduced group velocity. This light then propagates along the path of the fundamental mode of the resonator, where the resonator size has remained constant. This light then spends longer taking the same optical path as before a slow light structure was created. The light is then confined for an increased time, therefore leading to a larger Q-factor value. Then if we return to equation (12) it is possible to see that, for a fixed mode position (in terms of wavelength) the linewidth must decrease to compensate for the change in Q value.

$$\frac{1}{Q_{\text{total}}} = \frac{1}{Q_{\text{material}}} + \frac{1}{Q_{\text{radiative}}} + \frac{1}{Q_{\text{surface scattering}}} + \frac{1}{Q_{\text{coupling}}} \tag{14}$$

Let us return to the general consideration of the Q-factor now. It has been defined in terms of different properties but we have not yet considered the specific loss mechanisms from which it is determined. There are five loss mechanisms in WGMRs which are; absorption in the material, scattering in the material, surface roughness and dirt, curvature of the WGMR and coupling. Depending on the material chosen for the WGMR the loss due to material absorption will lead to a fundamental limit for the WGMs regardless of the shaping and polishing of the resonator. It is therefore good to choose a material with low absorption loss where possible. The presence of ions introduces a source of loss both in absorption (depending on the wavelength used experimentally of course) and also in scattering (Rayleigh). It is not possible, however, to avoid this for the given investigation. Equation (14) [14] gives the total Q-factor for a WGMR due to the contributions from

its loss mechanisms.

The first three terms of equation (14) are internal properties of the WGMR. The coupling component is due to how efficiently the energy from the incident beam is coupled into a particular mode (or modes) and can be broken down into mode matching as well as evanescent field overlap. Firstly the material loss will be considered.

As mentioned previously this is due to absorption as well as bulk Rayleigh scattering in the medium. It is one of the more significant contributors to loss in WGMRs other than surface scattering. It can be calculated as follows:

$$Q_{\text{material}} \approx \frac{4.3 \times 10^3}{\beta} \frac{2\pi n}{\lambda} \tag{15}$$

where β is the attenuation in dB, n is the refractive index of the WGMR and λ is the wavelength propagating in it. [18]

$$Q_{\text{Surface Scattering}} \approx \frac{3\lambda^3 R}{8n\pi^2 B^2 \sigma^2} \tag{16}$$

where; R is the radial radius of curvature, B is the correlation length and σ is the surface roughness. [12]

The radiative loss arises from the shape of the resonator. Since ideal TIR is considered for planar boundaries only, when TIR occurs on a curved surface not all of the light is reflected. A small portion of light leaks out at every TIR along the curved surface of the WGMR. For larger resonators the contribution due to radiative losses is quite small and equation (17) can therefore be used to approximate the loss it contributes. [14]

$$Q_{\text{radiative}} \approx e^{2m} \tag{17}$$

where m is the integer number of wavelengths in the resonator mode.

2.3.5 Coupling

Coupling to WGMs is achieved by the transfer of energy from the incident laser beam into resonant modes of the resonator. This can be done through free space coupling, where the laser is incident directly on the resonator. It has been found, however, that this method is not very efficient [14]. Coupling by an evanescent field is the most efficient method, with coupling efficiencies of close to 99% having been achieved [14]. Evanescent field coupling can be achieved a number of ways, such as; tapered fibre, angle-polished fibre or prism. With tapered fibres it is difficult to couple into high refractive index resonators, such as crystalline ones, since the fibre material requires a high refractive index. Creating tapered regions in fibres of this nature has not yet been achieved leaving non-fibre based coupling as the choice for crystalline materials, [14]. It is for this reason that prism coupling is

chosen and is the coupling method that is used in this experimental work.

This section explains the key considerations for mode coupling into WGMs. It will also highlight the angular dependence of mode coupling.

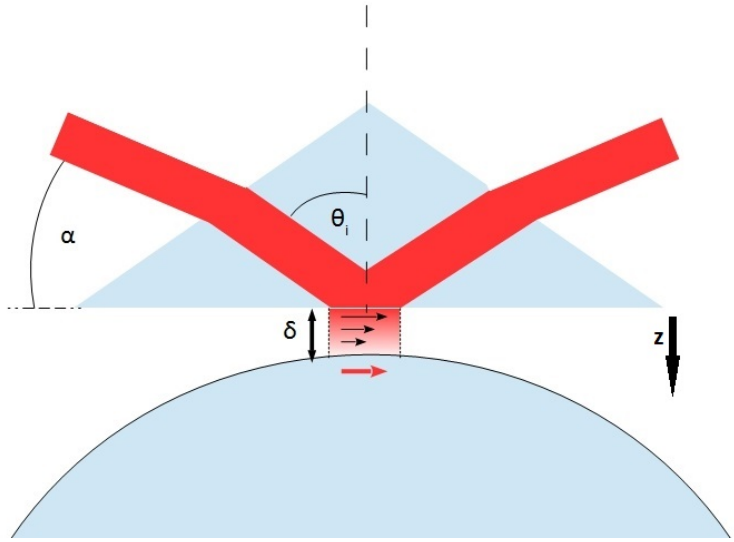

Figure 11: An illustration of the evanescent field generated between the prism and Whispering Gallery Mode Resonator. The horizontal black arrows indicate the direction propagation of the evanescent waves. Perpendicular to the prism back face the evanescent field decreases in intensity exponentially. This figure is based on a figure from [15]

$$\beta_m = n_1 k_0 \cos\theta - m \tag{18}$$

When an an incident beam is TIR on the back face of the prism coupler, close to a WGMR, an evanescent field is generated. The intensity of the field decreases exponentially in the z direction. If the WGMR lies within the penetration depth of the evanescent field for the given angle of incidence, the field will be frustrated allowing coupling of energy to occur due to the generation of a propagative wave. If the propagation constant of this propagative wave is equal to the propagation constant of a WGMR mode it has overlapped with then the system has been phase matched. This is equivalent to phase velocity matching and this is critical in order to achieve mode coupling. This is because when this condition is met, the light which has travelled through the WGMR is emitted back into the prism at the 'touch' point, the closest point between the prism and WGMR. Here the out-coupled light interferes with the TIR beam in the prism leading to destructive interference. If the intensities of the two beams, out-coupled and TIR prism beam, are equal and are out of phase by π, then critical coupling is achieved where there is 100% destructive interference between the beams. Since no energy propagates out of the prism in the regions where destructive interference occurs, these regions correspond to the modes. When critical coupling occurs, the depth of the resonances reach the zero baseline on the intensity scale. The phase matching condition is also angularly dependent as is shown by

the equation (18) [19] for the propagation constant, where θ_m corresponds to the mode angles. Therefore, as the incident angle varies the phase matching varies resulting in coupling to different modes which satisfy the phase matching condition. Additionally the penetration depth of the evanescent field, which is also angularly dependent, will vary changing the maximum possible energy transfer to particular modes at a fixed prism and WGMR separation. It is therefore possible to determine the most intense evanescent field using Snell's law. Figure 11 shows the evanescent field electric field decay in the z direction, i.e. perpendicular to the back face of the prism. The arrows parallel to the prisms face show that the that the propagative elements of the field, when frustrated, propagate in the positive x direction. The separation between the prism and the WGMR, in the z direction, should not be greater than the evanescent field penetration depth if good coupling is expected to be achieved.

$$\sin\theta \simeq \frac{n_r}{n_p} \tag{19}$$

where r is the axial radius of curvature of the WGMR and R is the radial radius of curvature of the WGMR. [12]

Additionally the considerations for efficient coupling consider two factors, the ideality and the criticality. The ideality of coupling refers to the ratio of the power which is coupled into a particular mode and the power of the incident beam. The criticality is concerned with the exchange of energy which occurs between the coupled light and the WGM at resonance. To achieve maximum coupling efficiencies the modal overlap should satisfy the following equation [12]:

$$cos\theta \simeq \sqrt{\frac{r}{R}} \tag{20}$$

$$r = R[1 - (\frac{n_r}{n_p})^2] \tag{21}$$

where n_r is the refractive index of the WGMR and n_p is the refractive index of the prism [12].

3 Experimental Coupling Procedure

This chapter details the stage by stage process of the experimental mode coupling to the WGMR. The details presented here, specifically for the coarse and fine mode coupling, will be referred back to later in chapters 5 and 6. Here the aim is to provide a detailed description of how to mode couple using a prism and its resulting evanescent field. The coupling described here was performed at the Max Planck Institute of Light in Erlangen, Germany. The equipment used is therefore the existing experimental setup from the group that was visited during this thesis work. The additional aim of this chapter is to gain knowledge of the equipment required for good mode coupling. Although no formal results were taken there are some photographs of various coupling traces, presented as examples, which are discussed in more detail both here and later in chapter 6. The chapter concludes with some short sections explaining how it is possible to determine certain coupling WGMR characteristics from the obtained traces. The Quality factor (Q), the Free Spectral Range (FSR) and the coupling efficiency are discussed as these are important parameters for the planned slow light measurements as changes in them are expected to result.
This chapter, along with the theory given in chapter 2, form the basis for the rest of the thesis. It provides the necessary knowledge to be able to imagine a design for use in a cryostat as well as for the preliminary experimental work at room temperature, discussed in chapters 5 and 6.

3.1 Experimental Setup

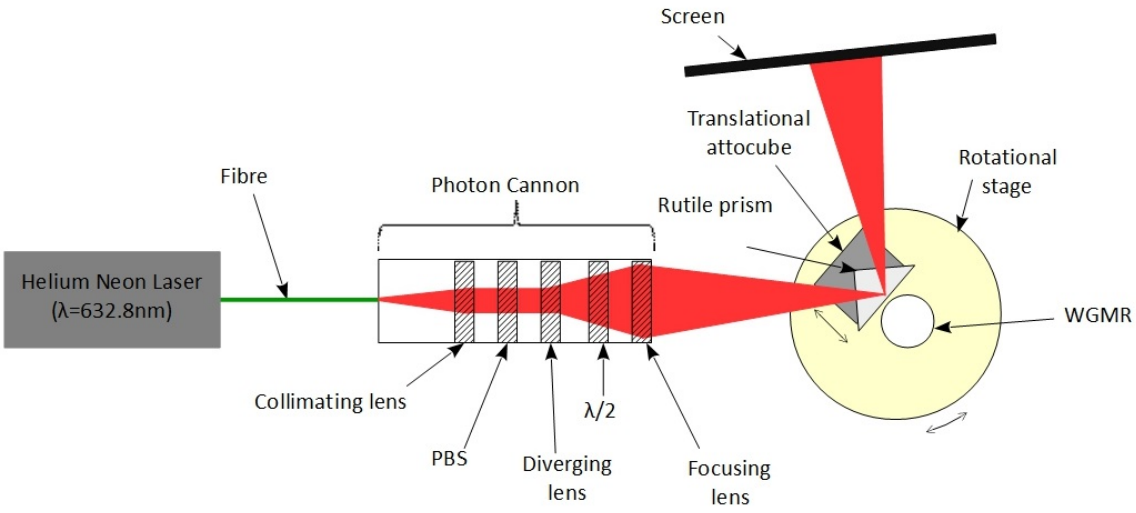

Figure 12: Schematic of the Coarse Coupling setup

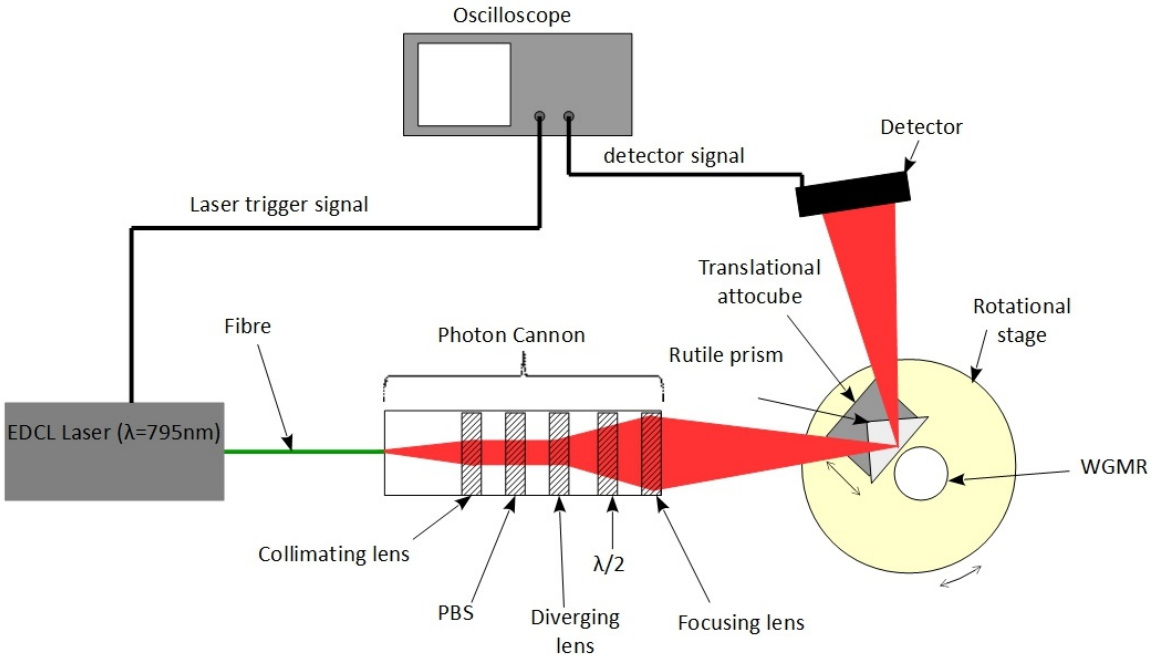

Figure 13: Schematic of the Fine Coupling setup.

Figures 12 and 13 illustrates the setups used. Two lasers, with fibre coupled outputs, are used in succession. The helium-neon (HeNe) laser provides visible light ($\lambda = 632.8$ nm) used to achieve initial, coarse coupling. The tunable external cavity diode laser ($\lambda = 795$ nm) can then be coupled such that a frequency scan is possible in order to optimise the coupling by looking for resonances.

The photon cannon is a series of optical components mounted in a cage system, used to ultimately produce a small focal spot for coupling into the WGMR. It consists of a collimator which collimates the diverging beam output from the fibre to a width of $\backsim 2-3$ mm. This is followed by a polarisation beam splitter (PBS) which allows only transverse polarised light to be transmitted. A diverging lens is then used in order to expand the beam size but it is less divergent than the fibre output. This is used to increase the coupling efficiency desired since a larger beam size through a fixed focal length focusing lens will lead to a smaller focal spot. The significance of the focal spot size will be elaborated on later in chapter 6. Finally the photon cannon contains a $\frac{\lambda}{2}$ to control the polarisation of the transmitted light and a focusing lens (focal length 15 cm) to focus the beam down to a small spot. The entire photon cannon is mounted on an x-y-z translation stage.
After the photon cannon, the beam is directed towards a rutile (TiO_2) coupling prism which is mounted on a linear translation stage which is electronically controlled, known as an attocube (the reader can find specifications in the appendix). The attocube allows fine control over the separation between the prism and the WGMR. The WGMR is mounted on a stand which is secured in a mount such that it is possible to adjust the vertical position of the WGMR. The attocube and subsequently the prism, as well as the WGMR stand, are all mounted on a base which sits on a rotational plate.

The TIR beam from the prism then propagates towards a screen or detector. The

screen and detector are put in each others place depending on the stage of coupling. The screen is used in conjunction with the HeNe laser to observe the interference pattern that arises at the boundary between the prism and WGMR, known as Newtons rings. The detector is then placed in the HeNe path before the fibre is changed to the ECDL fibre output. The infra-red (IR) beam is then detected by the detector, which is in turn connected to an oscilloscope such that the signal can be viewed.

The WGMR was measured to have a diameter of 4.14 mm and a thickness of approximately 1 mm. The WGMR is fabricated from a $Pr^{3+} : Y_2SiO_5$ crystal with a doping concentration of 0.05%.

3.2 Mode Coupling

To achieve high efficiency mode coupling, evanescent field coupling is used as described in chapter 2. Evanescent field coupling was achieved by using the above mentioned rutile prism coupler. The coupling is divided into two main sections; coarse coupling and fine coupling. The coarse coupling involves using the HeNe laser. This is because the coarse coupling involves observing the beam relative to certain components as well as an interference pattern, all done by eye. The laser wavelength therefore needs to be in the visible region of the electromagnetic spectrum. The fine coupling follows on directly after the coarse coupling has been realised. The fine coupling uses a tunable ECDL which operates in the IR region. It is possible to use a tunable laser of other wavelengths as well, the wavelength range is not of importance in this section simply the tune-ability. The reason for a scanning over a range of wavelengths will be discussed in more detail later in the chapter.

The first stage, once the equipment has been setup as per figure 12 using the HeNe laser, is to adjust the height of the WGMR with respect to the prism and the incident beam. The WGMR stand can be freed by loosening the screw holding it in place at the side. This way it is possible, by eye to ensure that the entire thickness of the WGMR lies within the height of the prism. The rutile prism used was several times taller than the WGMR was thick so adjustment of the WGMR stand was easily achieved. The beam then needs to be adjusted so that it will hit the WGMR at the correct height such that coupling at the closest point between the prism and WGMR is achieved. The beam should, when setup in the photon cannon, be ensured to be parallel with the optical table and therefore also with the prism and WGMR. To adjust for the height, the beam can be directed at the edge of the WGMR such that an image of the WGMR edge can be seen on the screen behind it. If the beam is not exactly at the edge then the entire photon cannon can be moved left or right until the correct position is found. It should be noted that the photon cannon is not fixed to the optical table at this point and so is free to be moved. When at the correct transverse position a streak of light should be seen, as illustrated in the photo in figure 14. The height can then be adjusted until this streak is horizontal.

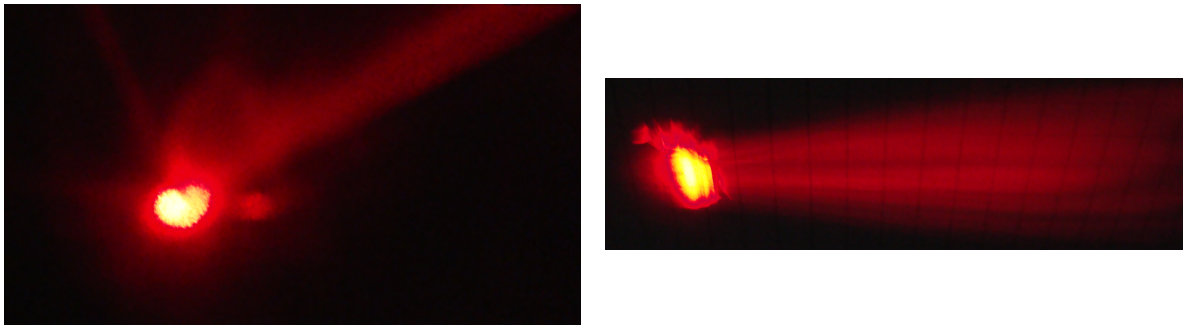

Figure 14: Photographs of the beam glare from the edge of the Whispering Gallery Mode Resonator. The image on the left shows the glare angled upwards which indicates that the beam is not at the correct height, relative to the Whispering Gallery Mode Resonator, for coupling to occur. The image on the right shows the glare to be horizontal which indicates the correct beam Whispering Gallery Mode Resonator height has been achieved.

The next stage of the coupling procedure is to coarsely couple into the WGMR; optimisation will be done later using the ECDL. Coupling is achieved only if the spacing between the prism and WGMR is correct. This means that the evanescent field of the WGMR mode and the evanescent field of the TIR beam in the prism should overlap. The optimum distance can be adjusted for in the fine coupling stages but for now it is sufficient to bring the prism to 'touch' the WGMR. The apostrophes around touch signify that the prism and the WGMR are not in fact physically touching but simply at a close enough position for coupling to occur. Experimentally this position is found by moving the attocube such that the prism is slowly moved towards the WGMR. Due to the way in which the attocube works when is moves using the continuous function a buzzing sound can be heard from it, equivalent to the frequency with which it is moving. When the prism is close enough to the WGMR, its oscillating movements will occasionally hit the WGMR causing a change in the audible frequency. When this frequency change is heard the correct position of the prism has been reached.

With the prism and WGMR distance adjusted such that coupling is possible it is necessary to correctly position the beam. The beam is focused due to the components in the photon cannon. Since the focal length of the lens is 15 cm the back face of the prism should be positioned approximately 15 cm from the focusing lens so that the beam waist is at the point of 'touch'. It is possible to check this distance either by using a ruler or by using a small piece of paper to follow the beam and locate the smallest point in the beam profile.

The final part of the coarse coupling is to correctly position the focal spot of the beam such that TIR occurs in the prism and so that the TIR point is at the point of 'touch', i.e. the closest point between the prism and WGMR. By calculating the incidence angle for the beam relative to the back face of the prism, a protractor can be used to help with approximate alignment. It is also noteworthy that choosing an angle slightly larger (circa 5 °) than calculated means that more modes can be coupled to making the fine coupling slightly easier. For this prism and WGMR the angle required was 59 ° for TE (42 ° for TM). TIR is easy to notice as the reflected beam will exit the prism through the third

face instead of going straight through the back face. The photon cannon (include translational stage) can be shifted in the traverse direction while observing the reflected beam on the screen, placed at some distance away from the prism. The beam size on the screen should be about 2 or 3 cm in diameter to make it easier to see the eventual interference pattern. The photon cannon should be moved in order to translate the beam until a Newton ring pattern can be seen as illustrated in the photograph in figure 15. Newton rings are an interference pattern which results from light reflected at the boundary between a spherical and planar surface. It is possible for them to occur as the results of particles of dust on the resonator surface. It is therefore necessary to confirm that the Newton rings seen are due to the interface between the prism and WGMR. It is possible to do this by observing the rings while moving the prism away from the WGMR using the attocube controls. If the rings disappear when the prism is moved away and reappear when the prism is moved back to 'touch' then these are to correct rings. When the rings have been found they need to be optimised such that the centre of the interference pattern lies in the centre of the reflected beam bright central spot. This is achieved by adjusting the knobs on the translation stage of the photon cannon. It is also the point at which the translation stage mounted photon cannon can be secured to the optical table. When this is done the beam position will change slightly so it is key to ensure that that Newton rings can still be seen at each incremental adjustment to secure the photon cannon. The knobs should be turned to compensate for the change in the beam position due to the clamping to the table. When the photon cannon is fully secured and the Newton rings are optimised the coarse coupling is complete.

To begin the fine tuning the detector should be put in the path of the reflected beam, still using the HeNe laser. The HeNe output fibre should then be detached from the photon cannon and replaced with the ECDL output fibre. The laser should then be set for a chosen central frequency and sweeping range. The sweeping range was set to 40 MHz. The output of the laser was coupled to the oscilloscope so that it could be used as trigger for the signal from the detector. The detector was coupled to another channel of the detector. The sweep of the laser could be seen on the detector as a positively sloped line and then a sharp negatively sloped line when the laser was quickly scanned back to the starting position.

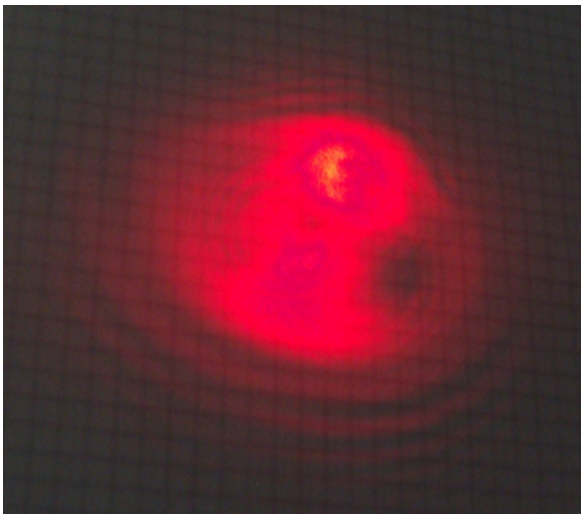

Figure 15: A photograph illustrating the Newton Ring pattern that results from the interference of the waves between the curved surface of the Whispering Gallery Mode Resonator and the flat face of the prism. This are used to indicate that the focal spot is in the correct position (at the 'touch' point) in order to achieve mode coupling.

When the laser scans over a frequency

which corresponds to a mode (resonance) in the WGMR a dip in the transmitted signal will be seen. This occurs due to the interference between the coupled light in the WGMR and the reflected light in the prism. Destructive interference occurs between them leading to a drop in the transmitted signal. If no dips are seen upon initial scanning after coarse mode coupling has been done then the beam position needs to be finely adjusted using the knobs on the photon cannon translation stage. Parameters should be adjusted one at a time so that it is possible to isolate the optimum position in each direction, x, y and z. When the coupling point is close to being reached the transmitted signal can be seen to start oscillating in such a way that it appears wavy. When this is seen along one parameter but no mode coupling is seen even when that point has been passed there is a good chance another parameter may need to be optimised. The original parameter should then be adjusted to return to this oscillating point before another parameter is adjusted.

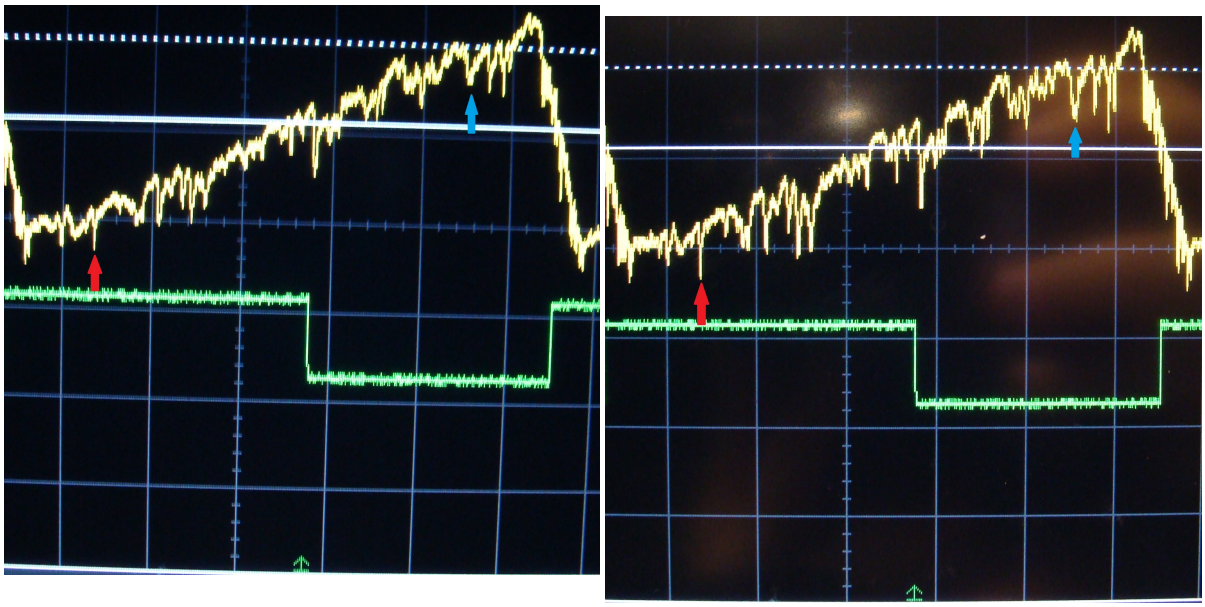

Figure 16: Photograph of oscilloscope traces showing mode coupling in the Whispering Gallery Mode Resonator for a fixed angle. The trace on the left is less critically coupled than the trace on the right. This is indicated by the lengthening of the modes coupled to in the right image compared to the left one where two example modes have been indicated with red and blue arrows, one colour for each mode. The vertical axis scale is 5 mV per division and the horizontal axis is equal to a sweeping range of 40 MHz

Figure 16 shows different stages in the fine mode coupling. When the mode coupling has been optimised by adjusting the x, y and z parameters such that the modes are as long and defined as possible the fine mode coupling is almost complete. The final parameter which can now be checked is the prism and WGMR separation. If the attocube controls are adjusted to move the prism closer or further away from the WGMR the mode coupled trace on the oscilloscope can be observed for any changes. If the separation is increased from the optimum coupling distance the lengths of the resonance dips should decrease. If the separation is decreased into the over coupled regime then the width of the resonance modes will increase. The optimum separation yields a mode coupled profile where the resonance dips are as long as well as, as narrow as possible. The criticality of

the coupling is then limited by other factors such as the focal spot size and shape which are not discussed further at this stage.

Once optimal mode coupling has been achieved for a fixed angle it is possible to reduce the angle size in order to couple to lower order modes. The ability to adjust the angle in order to meet the coupling conditions for different modes comes from the phase matching condition as stated in chapter 2. By reducing the angle it is possible to phase match the incident beam to lower order (fundamental) modes in the WGMR. When the angle of incidence is changed there is also a movement of the focal spot position as a result of a change in the optical path through the prism. In order to achieve optimal mode coupling for any new angle the focus position needs to be adjusted using the x, y and z positions of the photon cannon. The oscilloscope trace should be monitored while all the adjustments are made. It is also possible that the prism and WGMR separation needs to be adjusted as well since the penetration depth of the evanescent field is dependent on the incident angle. The change in the distance may, however, be smaller than the attocube movement resolution such that adjustment of the prism may not be required to achieve an improved result. It is still a parameter worth checking though. Figures 16 (a), (b) and 17 show pictures of the oscilloscope trace for different incidence angles.

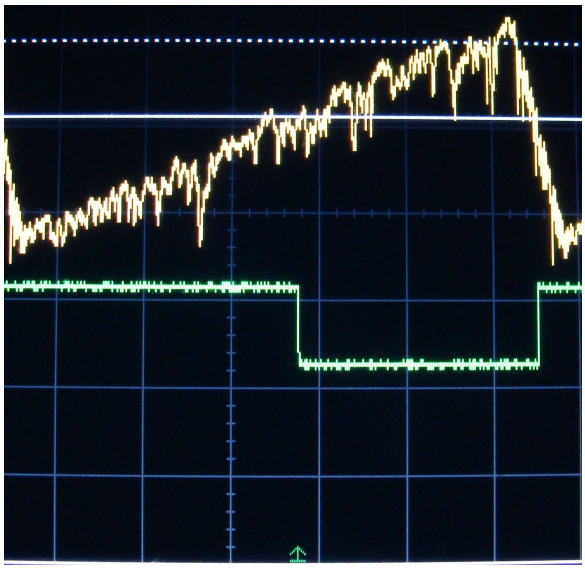

Figure 17: Photograph of an oscilloscope trace showing mode coupling in the Whispering Gallery Mode Resonator. The trace is taken for a change in the incident beam angle compared with the traces shown in figures 16(a) and (b). The vertical axis scale is 5 mV per division and the horizontal axis is equal to a sweeping range of 40 MHz.

An additional note which should be included here is ensuring that the reflected beam always hits the detector. As the beam is adjusted and similarly after the prism and WGMR have been rotated, the reflected beam position will change. This can be noticed by seeing a drop in the signal on the oscilloscope. The detector should then be moved so that the signal increases to a maximum value before further beam adjustments are made. It should also be ensured that, when the HeNe is initially focussed onto the detector,

the beam size incident on it is sufficiently small so that none of the signal is lost. If some of the signal is lost this will introduce errors in the Q-Factor and coupling efficiency determined from the oscilloscope traces.

3.3 Determining the Quality Factor

When optimal coupling has been achieved the oscilloscope trace can be saved for analysis. In order to be able to obtain numerical information about the Q-factor it is necessary to have calibrated scales for the trace such that the central wavelength of a resonance and its linewidth can be determined. It is then possible to calculate, for a chosen resonance dip, the Q-factor by using the equation (12) given in chapter 2. Figure 18 shows a photograph of relatively good mode coupling for the longest resonance located approximately in the centre of the mode trace. This value can then be compared to theoretically determined Q-factors for the WGMR.

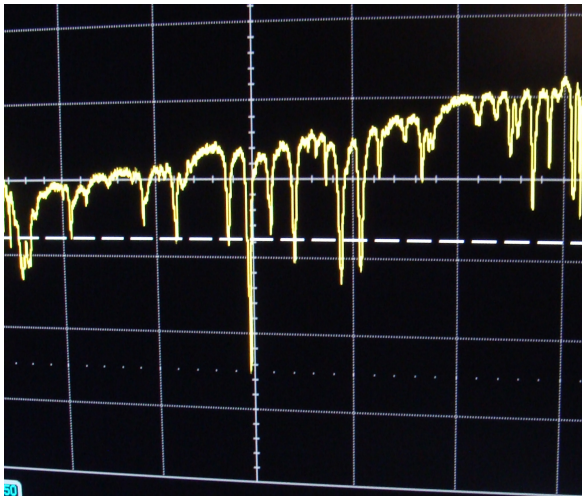

Figure 18: Photograph of an oscilloscope trace showing mode coupling in the Whispering Gallery Mode Resonator. The dips in the trace are regions where destructive interference has occurred between the light that has circulated around the resonator and out where it has met the totally internally reflected beam in the prism coupler. The vertical axis scale is 5 mV per division and the horizontal axis is equal to a sweeping range of 40 MHz.

When considering the experimental Q-factor it is also logical to determine the ideality of the coupling. The 'ideality' gives a measure of the 'parasitic coupling' to other, unwanted modes, [12]. The ideality is the ratio of the power coupled to the desired mode to the power coupled to all modes, inclusive of the mode of choice. It is clear from this term that highest Q-factors should be achieved when coupling occurs only to a single mode. For this reason using a coupler which can be tuned to select a specific mode should improve the efficiency of the coupling, provided that it can maintain the other desired coupling properties simultaneously.

3.4 Determining the Free Spectral Range

The FSR can be determined simply in one of two ways. Firstly it is possible to estimate the FSR of the WGMR using equation (22). It is then possible to choose a scan range which slightly exceeds this FSR in order to ensure that the true FSR lies within the scan trace. The trace can then be studied to locate the repeating mode pattern indicative of a FSR. For this WGMR the estimated FSR is 12.8 GHz.

$$FSR = \frac{c}{2\pi nR} \tag{22}$$

The second option, in the cases where either there is no frequency scale on the oscilloscope trace or the scan range is too narrow, is to introduce side bands.

3.5 Determining the Coupling Efficiency

The coupling efficiency is determined according to three parameters; the angle in the prism (i.e. the phase matching condition for a particular desired mode, the distance into the evanescent field (i.e. the criticality of the coupling) and the numerical aperture (i.e. how well matched the numerical aperture of the incident beam is with the numerical aperture of the WGMR mode. Experimentally it is determined from the length of the resonance dip and given in terms of percent. 100% coupling efficiency would result in a resonance dip which reaches all the way down to the signal baseline, indicating total destructive interference has occurred for that frequency.

4 Proposed Holder Design for Cryostat

This chapter discusses the individual considerations required in order to perform WGMR mode coupling within the confines of a cryostat. The reason for needing the cryostat was mentioned in section (2.1.3) regarding phonon broadening no longer being dominant at low temperatures, such that it is possible to target a specific hyperfine transition and perform SHB. The cryostat considered for use here will be operated at temperatures around 4 °K (or -269 °C). The chapter will start with a brief overview of the required geometry of the setup including a schematic of the cryostat to provide information about the size restrictions. The prism and attocubes required to achieve the required beam path through the cryostat and the control of the component positions, for coupling, are then discussed. There is a brief discussion about the need for appropriate adhesives to attach the prism and resonator to their respective base and stand where some good and bad suggestions are given along with reasoning for their prospective use. The chapter concludes with a holder design which is capable of meeting the requirements, where the section is divided into the inner and outer frames, for simplicity.

4.1 Geometry

The central consideration with the geometry are the conditions required to achieve coupling to the WGMR. As explained in the theory in chapter sections 2.2 and 2.3, TIR in the prism coupler is needed to generate an evanescent field and this field then needs to be adjustable in space such that it can overlap with the evanescent field of the WGM or modes to couple to. Additionally adjustment of the angle of the incident beam with respect the back face of the prism is needed to be able to control the phase matching of the beam and the WGMR mode(s) to allow for the possibility to select which mode(s) to use.
The second consideration is the creation of slow light structures. For this, cryogenic temperatures are required and as such the coupling needs to be performed in a cryostat. The dimensions of the cryostat and cryostat chamber impose restrictions on the setup and what components can be used inside the cryostat as well as what optics can be used out with the cryostat, including any limitations on the beam that might be incurred.
Figure 19 shows a rough sketch of the requirements for the geometry of the setup.

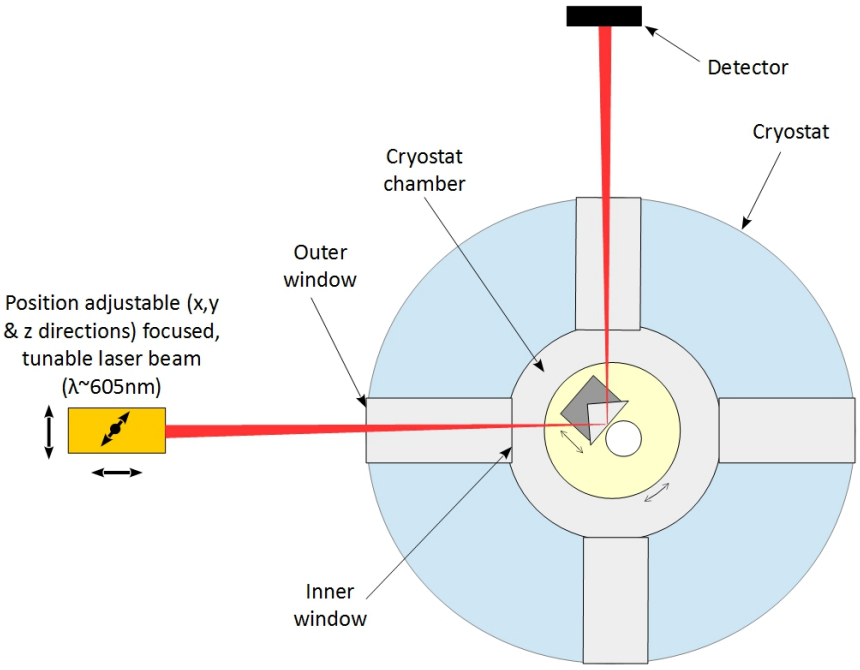

Figure 19: A schematic (not to scale) of the setup geometry using a cryostat. The Whispering Gallery Mode Resonator and prism are located in the centre on the cryostat, in its chamber. The beam has access to the Whispering Gallery Mode Resonator and prism setup via four windows, of which two are used for in- and out-coupling.

4.2 Prism

The prism needs to be shaped in such a way that it can meet two specific requirements. It must be possible to achieve TIR on its back face at an angle, or range of angles, such that mode coupling can be achieved, ultimately with the aim of fundamental mode coupling only. The second requirement is that the incident and reflected beams should be able to enter and leave through two different cryostat windows for all cases within the range of angles that the WGMR and prism setup are rotated through. These restrictions will impact which angles the prism corners can have, although the lengths of the faces and the height of the prism are also properties which need to be determined with motivation.

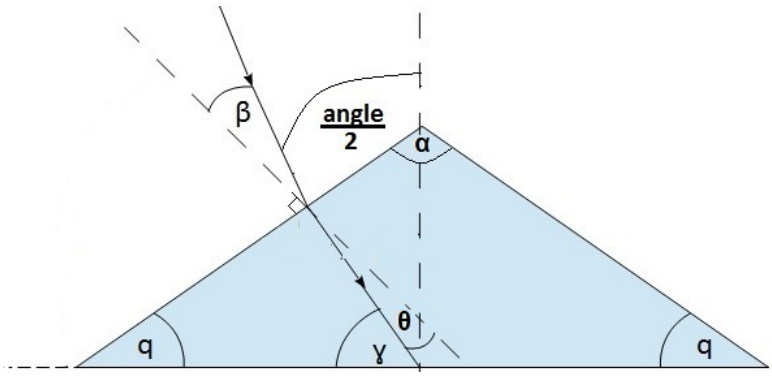

Figure 20: Angles influencing the geometry of the prism and incident and reflected beams. From the figure, it is possible to see how to determine the internal prism angles which result in an angle of 90 ° between the incident and reflected beams. This is required so that the beam can enter and leave the cryostat windows without being clipped or blocked.

Using Snell's law both for the initial refraction of the incident beam on the first face of the prism and then under the TIR conditions on the back face of the prism, at the coupling boundary, the corner angles of the prism can be determined. Since the cryostat windows are all at 90 ° to each other the prism shape should be chosen so that the incident and reflected beams enter and leave the prism at 90 °, or as close to 90 °, as possible, with respect the the incident and exiting prism faces. Figure 20 illustrates the geometry prism where the angles of interest are marked. The computational code for solving the problem can be found in the appendix. The relevant results, i.e. around 90 °, of the calculations are given in the table below. The critical angle for the prism and WGMR boundary was calculated using equation 5 and was found to be 48 °. The incoming prism face boundary was then considered for the situation in the cryostat, i.e. for liquid helium and diamond. These are the two refractive indices defined in the code in the appendix. β is the chosen to be looped from $0 - 90$ ° in order to provide a solution to Snell's law so θ can be determined and subsequently be used to determine the corresponding α. The fourth column of the table below gives values for the 'angle' between the incident and reflected beams. When this value is equal to 90 ° the corresponding value for α can then be used to define the internal angles of the prism.

β	θ	α	angle
1.80	0.76	85.53	89.13
2.00	0.85	85.70	89.70
2.20	0.93	85.86	90.26

Table 1: A table of the different angles in the prism geometry in order to find the appropriate inner prism angle so that the incident and reflected beams, when totally internally reflected, have an angle between then of 90 °, or as close to this as possible. The column headed 'angle' refers to the angle between the incident and reflected beams. α is the internal prism angle determined. β is the angle of the incident and reflected beams with respect to the normal of the prism faces they enter and exit.

Unlike the prism in chapter 3, a diamond prism is chosen for use in the further setups. The rutile (TiO_2) prism is birefringent so eliminating this polarisation dependence of the prism simplifies the coupling setup. The diamond prism can also be fabricated to be small making it more convenient for use in the confines of the cryostat chamber. The diamond prism has inner angles of 47.11 °, 47.11 ° and 85.78 °. The long (back face) is 2.5 mm in length and 1.5 mm in height. The other faces are both 1.84 mm long and 1.5 mm in height. The edges are chamfered making small facets of 0.05 mm in size.

4.3 Attocubes

Two attocubes are required as part of the cryostat setup. As was discussed in chapter 3 (section 3.2), two movements of the WGMR and prism setup are required to control the coupling. Adjustment of the prism and WGMR separation distance allows the overlap of the evanescent fields of the prism and WGMR to be controlled. Being able to rotate the prism and WGMR setup such that the incident angle of the beam with respect to the back face of the prism can be reduced leads to control over which modes can be coupled

to, as per the phase matching condition discussed in 2.3.5.

The lateral movement should be achieved by using the ANPx51 attocube (full specifications can be found in the appendix - [16]), as was done in chapter 3 and similarly is used for the room temperature measurements done in chapter 5. The dimensions in mm of this attocube are maximally 15×18 and at a minimum 15×15. Since the prism does not need to be moved the full 3 mm during the coupling procedure it is also possible to gain space by not using the full range of the attocube during experiments.

The full specifications of the attocubes can be found in the appendix and additionally on the company website for attocube, [16].

4.4 Adhesives

Due to the contraction of the components an appropriate adhesive needs to be selected so that detachment or stress or strain occur, leading to damage of the WGMR and prism. A study into possible choices should be made where how their properties between 24 °C and 4K are known. They need to be strong enough to secure the prism and WGMR to their respective mounts and matched to the contraction and expansion properties of the mounts, prism and WGMR respectively.

4.5 Holder

The holder should be able to fit into the cryostat chamber comfortably and contain within it the two attocubes, the prism and the WGMR. Due to the maximum load capabilities of the attocubes, each part of the holder must also be lightweight but robust, so as to reduce oscillations from either movement of the attocubes or the liquid helium flowing around in the chamber. In order to be able to apply any eventual magnetic field, which may be of interest in future experiments, it is also necessary that the parts are non-magnetic.

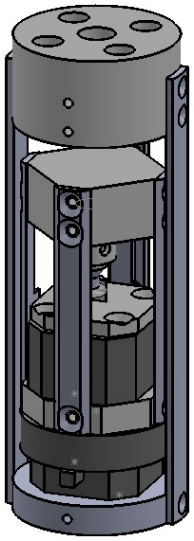

Figure 21: Solidworks model and drawings of the proposed cryostat holder.

PEEK (Polyether ether ketone)in combination with a non-magnetic steel have been used for numerous cryostat compatible crystal holders within the QI group at Lund University. These are therefore the two

materials of choice for constructing the holder and additionally PEEK is also lightweight.

The holder is made up of two separate frames which are placed one inside the other and joined together. The outer frame is stationary with respect the the cryostat windows and the inner frame can rotate about the vertical, y-axis. The following two sections will address each of the frames separately, detailing the structure and operation of them.

Figure 21 shows the proposed holder design for use in the cryostat. All the solidworks drawings are to scale and the dimensions are given in millimetres. A complete collection of the individual components of the holder can be found in the appendix. All the holder parts are attached together using non-magnetic screws, with the exception of the WGMR and prism, which are both attached to their respective mounts using adhesive.

4.5.1 Inner Frame

The inner frame holds the prism, WGMR and the translational attocube (ANPx51). Unlike the original coupling setup outlined in chapter 3 and also used later in chapter 5, the WGMR and prism are not mounted from the same plane. This arises from the fact that the entire system needs to be able to rotate in order to control which modes are coupled to; however, only one of the components, the WGMR or the prism, needs to be translated horizontally to achieve evanescent field overlap. The close confines of the cryostat chamber along with the restrictions imposed by available attocubes, i.e. the ANPx51 is the smallest translation attocube available, led to the repositioning of the WGMR relative to the prism.

As can be seen in figure 22 the WGMR is suspended from the upper part of the frame with its rim 'contact' point positioned at the centre of the rotation. Of course the WGMR could have been chosen to be attached to the ANPx51 attocube instead of the prism, however, because of the convention set earlier in the thesis, the prism was chosen to be mounted on the attocube. This arrangement means that the maximum space required in the horizontal plane is equivalent to the maximum range of the attocube plus the thickness of the supporting bars, with some additional space in-between to ensure the attocube functions correctly.

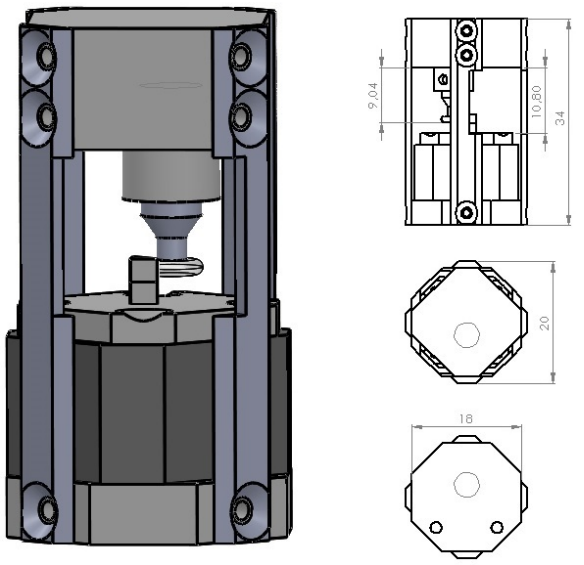

Figure 22: Solidworks model and drawings of the inner frame of the proposed cryostat holder. All dimension are to scale and are in millimetres.

The prism can also be seen mounted on

a raised portion of a base plate, secured to the top of the attocube (ANPx51). This is useful for two reasons. Firstly, it allows some space below the WGMR such that the position, vertically, can be adjusted both upwards and downwards as required. This may not seem immediately necessary as the WGMR rim should be aligned precisely with the back face of the prism, which seems like an arbitrary task. When in room temperature this is true since the WGMR stand and mounting plate for the prism will not experience any expansion or contraction due to temperature. When the holder is, however, submerged in the liquid helium within the cryostat chamber all the components and holder parts will experience some contraction due to the large temperature difference around 290 °C. Subsequently any initial alignment of the prism and WGMR will need to take the eventual contraction of the mounting plate and WGMR stand into account.
The second reason that the raised prism mount is useful is to ease coupling. If some extra height is given alone to the portion where the prism sits it will simply slightly the adjustment of the incident beam height in the case that it may not be 100% horizontal. This will give some allowance for initial coupling where neither the incident nor the reflected beams are 'clipped' by the base plate.

The entire inner frame is mounted on a rotational attocube (ANR51), who's stationary part is mounted to the outer frame. The rotational attocube performs the same role as the rotational stages in both chapter 3 and 5, provide, of angular mode tuning.

The bars of the inner frame are indented so that the reflected beam, due to any rotation of the frame, will not be obstructed as its angle changes. Similarly the indents mean the incident beam will not be obstructed by the bars as the frame rotates. Since the beams will pass through only two of the cryostat windows it is only necessary to indent three of the bars which, under any rotation of the inner frame, will begin to obscure the windows and thus potentially block or cut the beams. The central bar, between the two cryostat windows, has indents on both sides so that rotations in both directions can be compensated for. The right hand bar has an indent only on the left and vice versa for the left hand bar. In this way the indent is only on the side which will be rotated in front of the cryostat windows.

Finally, the reason for the inner frame being placed on top of the rotational attocube as opposed to hanging from it stems from the way the attocube is fabricated. Initial designs had the inner frame hanging, which greatly simplified the holder design; however, the ANR51 only has screw holes on one side of the rotation plate. This results in any load hanging from it pulling slightly on the screwed side causing a tilt in the rotating plate. This could cause problems operating the attocube since with any tilt there is a misalignment of the prism and WGMR with respect to the beam. As the attocube is rotated the misalignment would result in extra compensation in the movement of the focal spot position, with the need for control over the tilt of the beam, both vertically and horizontally. It was therefore decided that mounting the inner frame on top of the rotating plate would simplify the setup in terms of coupling into the WGMR.

4.5.2 Outer Frame

The requirement of an outer frame results directly from the previously mentioned tilt of the rotational plate of the ANR51 if the inner frame were to be mounted hanging from it. The holder is positioned into the cryostat chamber by means of mounting it on a long bar so that it can be fed down into it from above. Since the inner frame needs to rotate and be mounted on top of the ANR51, it is not possible for it to be directly attached to the bar. The outer frame must therefore provide a structure on which the ANR51 can be mounted while also providing a connection to the bar so that the holder can be fed into and removed from the cryostat chamber. The Solidworks model and drawings of the outer frame are presented in Figure 23.

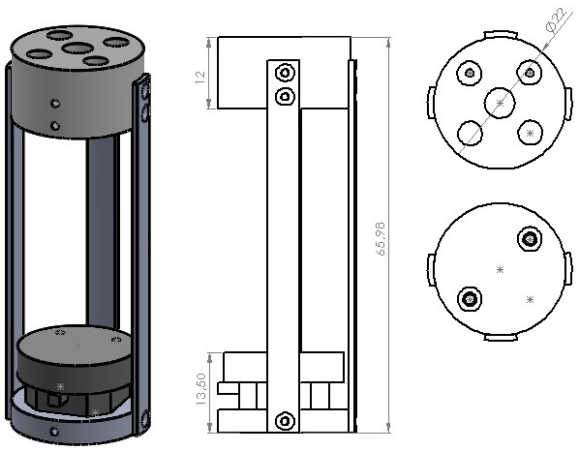

Figure 23: Solidworks model and drawings of the outer frame of the proposed cryostat holder. All dimension are to scale and are in millimetres.

Due to the size restrictions of the cryostat chamber and the dimensions of the inner frame, the outer frame design is directly dependant on these two factors. The ANPx51 has a minimum footprint of 15×15 mm and its top plate can be translated 1.5 mm in the forward and backward directions. Since the separation between the prism and WGMR is on the order of micrometers to achieve coupling, the translation of the prism position does not need to be large. As a result it was decided that a maximum footprint for the ANPx51 could be 17 mm when used in this setup. This provides the outer frame with an additional millimetre of space. Since the attocubes require a small amount of space around them to ensure correct operation, the reduction in the translation of the ANPx51 can be used to provide 0.5 mm of space on either side of the attocube. This means that the space occupied by the inner frame, with the additional 1 mm of space, is 20 mm where the thickness of the bars has been included. The diameter of the cryostat chamber is circa 25 mm so 5 mm remain to fit the outer frame. The base plate of the outer frame is therefore made to be a circle with a diameter of 22 mm such that bars can be fixed to the outside of it. This then provides 1 mm on either side of the inner frame to allow space for it to rotate without hitting the outer frame bars. The bars of the outer frame also need to be sturdy enough to support the entire structure however simultaneously they need to be thin, in order to fit in the cryostat chamber. For this reason steel is chosen with a thickness of 1 mm. The width of the bars have been calculated so that they are the same size as the spacing between the cryostat windows. Since they do not move once the holder is in place in the cryostat, they will not block the windows. Only three bars are used so that the ANR51 (with feedback) attocube is able to fit since it has an additional feedback feature on one side.

5 Whispering Gallery Mode Resonator Characterisation

In order to be able to assess the effects of slow light in the WGMR it is necessary to achieve optimum mode coupling under normal operating conditions. In this context, " normal " is defined as coupling at a stable room temperature (24 °C), where no SHB is performed. It is vital to optimise the beam alignment as well as the size and shape of the beam focus (ideality of coupling). Additionally, other effects are of interest in the determination of the best experimental conditions in order to achieve the deepest resonance dips (criticality of coupling) and also the narrowest resonance dips (lowest loss), such as absorption and fluorescence. For this reason two beam alignment schemes are tested with consideration of both the quality of the results possible as well as the ease of use. When the experiment in the cryostat is performed it will be made more complicated by the restrictions in viewing the WGMR and prism assembly as well as the dimensions of the cryostat.
The two different coupling regimes used in this chapter are; free beam coupling and fibre coupling. The subsections are less focussed on the stage by stage details of the coupling since this was already discussed previously in chapter 3. Instead the manipulation of the optics is discussed, including any new details that were not present or differ from the coupling in chapter 3 and the two coupling stages; coarse and fine coupling are used instead. These terms correspond to the same stages described in chapter 3. Results, in the form of oscilloscope traces, are taken under various conditions and later presented and discussed in chapter 6.

5.1 Equipment

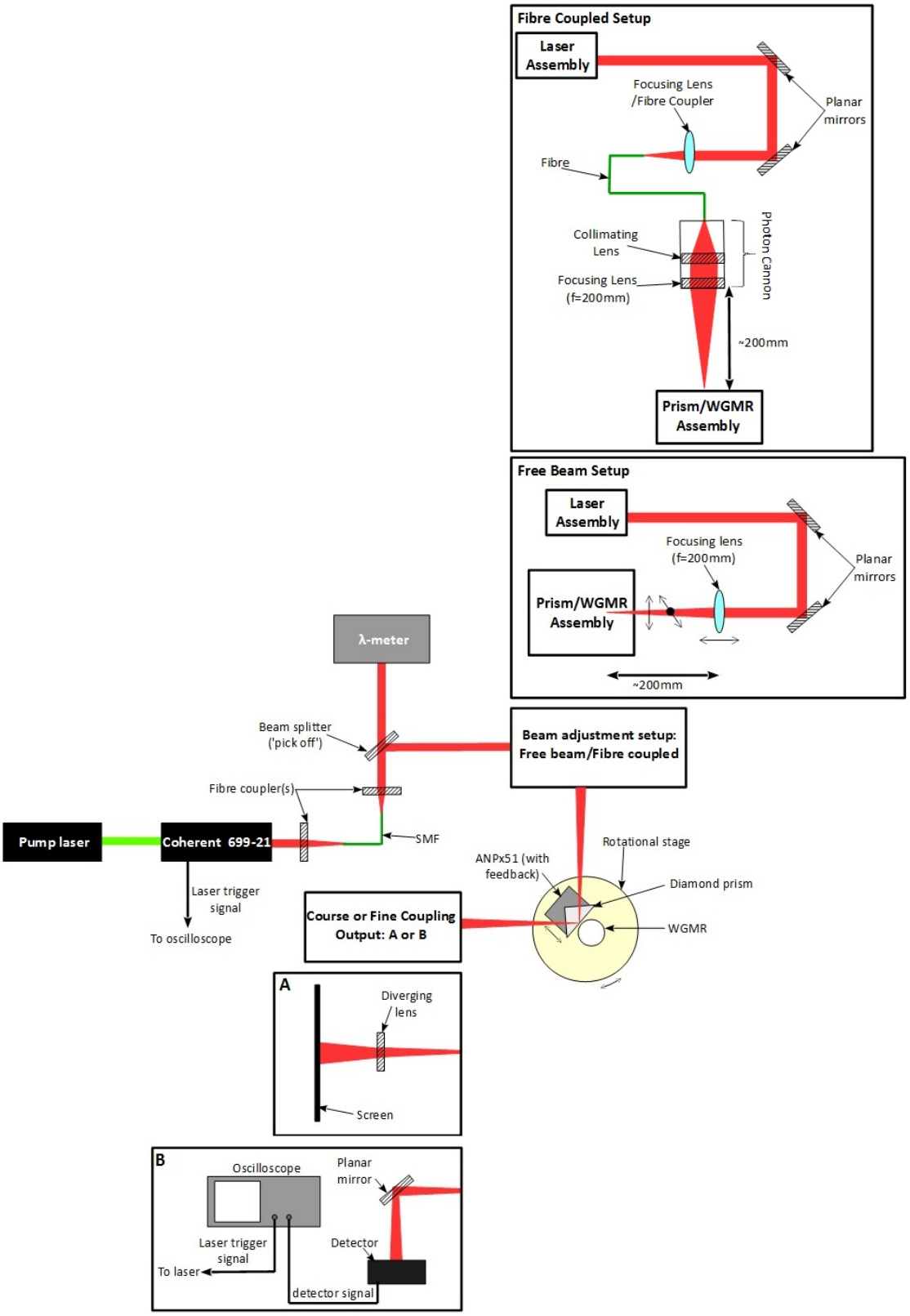

Figure 24: A schematic of the coupling setup with boxed regions illustrating the free beam and fibre coupled setups as well and the coarse and fine coupling out regimes (A and B).

Figure 24 shows the schematic of the setup used for the WGMR characterisation measurements. A $Nd:YVO_4$ solid state laser is used to pump a Coherent 699-21, tunable ring dye laser(λ range $= 590 - 610$ nm). The output of the tunable laser passes through single mode fibre (SMF) which 'cleans' the beam so that only the 00 mode propagates. At the 'pick off', a beam splitter, the beam is directed to a wave-meter and to one of two different setups; free beam and fibre coupled, which are the two different approaches used for mode coupling. The beam from each of these setups is then incident on the diamond coupling prism (n=2.419) where it is then evanescently coupled into and out of the WGMR. The reflected beam from the prism is then directed initially at a screen, for coarse coupling, via a diverging lens and then later at a mirror which directs the beam towards the detector for the fine coupling. Finally the signal from the detector, as well as the trigger signal from the laser, are coupled to an oscilloscope where the mode coupling trace (interfering reflected prism and out-coupled WGMR beams) can be viewed.

5.1.1 Tunable Laser

A Coherent 699-21 tunable ring dye laser was used for coupling to the WGMR. The laser was set to scan around selected wavelengths for scan ranges of 15 GHz for the free beam measurements and 9 GHz for the fibre coupled measurements.

To observe mode coupling in the WGMR the ability to scan over a range of frequencies is required. The tunable laser provides this function through the peizo controlled oscillation of the thick etalon, which varies the cavity length and thus the preferential lasing resonances of the cavity. By adjusting the birefringent filter, using the knob, it is possible to tune the wavelength of the laser. The laser wavelength output is monitored by a wave-meter, connected to the computer, which is fibre coupled to after one of the 'pick offs'.

If the wavelength chosen lies at the boundary between mode families of the laser cavity when scanning the laser it is possible that mode hops occur. To avoid mode hops the wavelength of the laser can be tuned, with the birefringent filter, until a peak in the output is found. If this fails to resolve the problem then the scan range will need to be reduced.

5.1.2 Holder

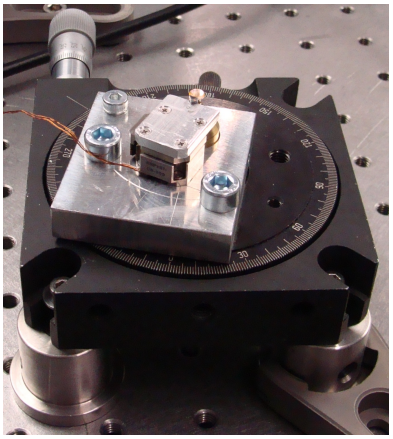

Figure 25: A photograph of the holder used for the free beam and fibre coupled setups. The holder is seen mounted on top of a rotational stage. Attached to the top of the holder is the translational attocube (with feedback), the Whispering Gallery Mode Resonator (mounted on a metal stand) and the diamond prism.

A holder for the prism and WGMR, which can be mounted on a rotational stage, was required. Figure 25 shows a photograph of the holder from above and from the side, with some added dimensions. The design places the 'touch' point of the WGMR rim as close to the centre of rotation as possible. This was chosen to reduce the adjustments in the beam focus when the system is rotated. The WGMR is mounted on the same stand as in chapter 3 and the hole for it is positioned so that it goes through the centre of the rotational stage in order to be able to control the WGMR height relative to the fixed height prism. The WGMR stand is secured with two screws from the side.

There are two threaded screw holes, M1.6, in order to mount the ANPx51 attocube. A metal plate with four 1.7 mm holes is attached to the top plate of the attocube. The plate serves two functions; to be able to remove the prism without removing the adhesive (wax) and secondly to extend the reach of the prism so that it can get within coupling distance of the WMGR. Since the maximum distance the attocube can be moved in a single direction is 1.5 mm, this would require the edge of the attocube base to be within this distance from the 'touch' point of the WGMR rim. Due to the shape and dimensions of the WGMR stand this is not possible. The asymmetric plate therefore provides the extra distance required and even means that the full 1.5 mm does not need to be travelled in order to reach the coupling distance. The base of the plate, between the nearest screw holes to the WGMR and the edge, is sanded away at an angle to provide access on approaching the WGMR. This is again due to the shape of the WGMR stand.

Both the WGMR and the prism are attached to their respective mounts using wax. This means that they can be removed by gentle heating, with any excess wax able to be removed using acetone. It should be noted that the prism was originally attempted to be fixed to the plate using silver paint but this proved not to provide a strong enough adhesion.

The rotational stage, with the holder and other components mounted on it, is raised off the optical table using three metal legs. The heights of the legs can be adjusted as required during the alignment process.

5.2 Free Beam Setup

In this section the first of two different beam alignment methods for coupling is discussed. Figure 24 illustrates the complete coupling setups for coarse and fine coupling. Figure 24 shows the beam alignment portion used for the free beam setup. As can be seen in the figure, two planar mirrors are positioned after the 'pick off', perpendicular to each other, and are used to adjust the beam height and lateral position. A focusing lens with focal length of 200 mm is positioned after the second mirror to focus the beam down to a spot within the prism. The incident beam , on the lens, has a diameter of circa 2 mm leading to an estimated focal spot diameter of 76 µm. The prism and WGMR assembly is then positioned circa 200 mm from the centre of the focusing lens, measured roughly using a 30 cm rule.
The beam is firstly aligned with respect to the optical table. Adjustments are made in the angles of the two mirrors to make the beam parallel to the optical table and at the same height as the WGMR. The alignment is checked using the same rule as before. The mirrors are also adjusted to ensure that the beam is perpendicular to the lens so that its focal spot shape is not distorted when it passes through it. When the beam is satisfactorily aligned the coarse coupling, as previously detailed in chapter 3, can be done.
The coarse coupling, in the case of the free beam coupling, needs to be performed in a slightly different way since there is no photon cannon which can be moved. As a result the WGMR and prism assembly is instead not fixed to the table, until coarse coupling has been achieved, and is subsequently moved by hand to find Newton rings. Of course the attocube, which the prism is mounted on, has been adjusted such that the prism has been brought to 'touch' the WGMR before coarse coupling is started. Also unlike chapter 3, the prism being used is made from a different material and is also much smaller in size, see chapter 4 for the dimensions. The smaller dimensions of the prism mean that the vertical adjustment of the WGMR, with respect to the prism, needs to be more precisely done. When the Newton rings are seen on the screen the WGMR and prism assembly can begin to be secured to the table carefully, where the mirrors are adjusted to compensate for the change in position of the assembly in relation to the beam. The beam is directed at the prism at an angle estimated as slightly larger than 90 ° as per the calculations in chapter 4.
When the coarse coupling has been achieved a planar mirror is placed at the output of the prism such that the beam can be directed at the detector. The laser is then swept over 15 GHz for a sweep time of 0.25 s. The wavelength is initially set to 600.2 nm since mode jumping was encountered at both 607 nm and 602 nm. These wavelengths all lie within the absorption range of the Pr^3+ ions, given by the absorbance spectrum found in the appendix. It is this range that will be used when SHB and is therefore the region of interest for initial, room temperature (24 °C) measurements.
Once the laser has been set to sweep, the oscilloscope trace can be viewed in order to

begin fine coupling. As detailed in chapter 3 the trace, if no modes are initially visible, is studied for a wave like oscillation that occurs near the coupling point. The mirrors controlling the incident beam are carefully adjusted and the lens position is moved to compensate for the change in beam position. The lens can also be moved backwards and forwards along the direction of travel of the beam to vary the depth of the focus. The trace is monitored for 'beam walks' along the lateral and vertical directions and mode traces are saved from the oscilloscope. For movements in the beam position, the resulting beam incident on the detector varies. The mirror after the prism is therefore adjusted to ensure the beam is always incident on the detector. Due to the low efficiency coupling observed at the initial wavelength, no measurements for different wavelengths were recorded for analysis although they were checked. The results can be found in chapter 6 where the coupling process is discussed in more detail along with the mode traces.

5.3 Fibre Coupled Setup

This subsection details the fibre coupled beam adjustment setup. The fibre coupled setup was assembled and used in an attempted to improve the coupling results in comparison to the free beam setup. It was also found that maintaining alignment of the optical components as well as the ease at which changes in the mode structure could be seen in the previous setup were troublesome. The fibre coupled setup mimics the setup used in chapter 3 where a photon cannon system, with fewer components, is assembled and used, mounted on a translational x-y-z stage. The intention of this system is simplification of the beam position adjustment as well as improved accuracy of the alignment of the beam through the lens, therefore an improved focal spot shape. This is ultimately intended to reduce the losses in the coupling and improve the resonance dip shapes.

The first step of the fibre coupled setup requires the incident beam, from the 'pick off', requires redirecting into an optical fibre. The two mirrors used in the previous setup are used to align the beam into the fibre via a fibre coupler (focusing lens). The power before the fibre input was measured to be circa 380 µW using a power meter. The power meter is then placed at the output of the fibre to monitor the fibre coupled light. To couple the light into the fibre the fibre was initially pulled out of the holder such that the beam diameter covering it is enlarged. The beam can also be roughly aligned before this stage by observing the output through the holder aperture on a piece of black card. The fibre is then slowly and carefully guided back into the holder while the mirrors are adjusted to maintain a power output signal and increase it. Due to the long length of the fibre the coupled fibre power is expected to be around 30% as optimum coupling. With the fibre coupling complete a power output of circa 110 µW was recorded which was deemed sufficient for the mode coupling.
The fibre output was attached to the photon cannon. The photon cannon consists of a cage system of optical components mounted on an x-y-z translation stage. The diverging beam from the fibre was collimated using the collimating lens placed after it. Due to the large spacing the beam was able to diverge beyond the original in coupling beam diameter, resulting in a collimated beam diameter of circa 10 mm after the first lens. The same focusing lens (f=200 mm) as was used in the previous setup was fixed to the

output end of the photon cannon. The resulting focus spot diameter was circa 15 µm, the significance of which will be elaborated upon in the following chapter.
With the photon cannon setup the coarse and fine coupling stages were done. The WGMR and prism assembly were secured to the table after the relative heights of the WGMR and beam were performed. The photon cannon could then be manipulated, as was done in chapter 3, in order to look for the Newton rings. Similarly to the previous experimental sections, the prism was moved to 'touch' the WGMR. The Newton rings, as shown in figure 15, were significantly easier to achieve and clearer in form than had been achieved with the free beam setup.
The fine coupling stages are progressed to upon finding the Newton rings. The laser is swept over a range of 9 GHz for a sweep time of 0.25 s. The reduced frequency range was used due to mode jumping of the laser sweep for 10 GHz and above. This is less than the approximated FSR (12 GHz) of the WGMR which means the mode traces will not show the FSR, which makes analysis of the results more problematic but this will be discussed in the following chapter. The initial wavelength was 593.8 nm. The oscilloscope trace was then monitored while the photon cannon was translated in the x-y and z directions respectively. When the mode trace has been optimised, i.e. narrowest and deepest resonance dips, the trace is saved for analysis. The prism is then moved away from the WGMR until coupling is no longer visible on the oscilloscope and the trace is then saved. The prism is then moved back to 'touch' and another trace is then saved. This is repeated for a range of different wavelengths; 600.5 nm, 606.2 nm and 610.4 nm, so in order to provide information about the potential influence of absorption loss at the different wavelengths. All the beam settings are kept constant for the different wavelengths.
A second set of data for a range of wavelengths was then taken however with the beam position adjusted to see if better coupling could be achieved for the different wavelengths. The data was recorded for a larger range of wavelengths; 593.1 nm, 595.2 nm, 596.2 nm, 597.6 nm, 598.9 nm, 600.5 nm, 603.7 nm, 605.4 nm, 606.2 nm, 610.1 nm and 610.4 nm. The results are presented and evaluated in the following chapter.

6 Results, Analysis and Evaluation

This chapter presents the results of the two mode coupling beam setups employed in this thesis. The manipulation of the beam position using each of the setups, in terms of problem areas and ease of use, are also discussed. This chapter aims to give an indication of the optimal setup for use in the future experiment involving the cryostat. The results are also discussed with reference to the rough results obtained in chapter 3 in terms of the coupling efficiencies achieved. An estimated spot size for optimal coupling is calculated and used to motivate the interpretation of the results as well as the need for a more extensive investigation. The significance of the absorption at different wavelengths is also discussed where the absorbance spectrum of the ions motivates a proposed trend that is expected. The results and subsequent discussions presented here aim to provide a basis from which to continue optimising the experiment to investigate slow light effects in WGMRs.

6.1 Free Beam Setup

In this sub-chapter the results from the initial setup are presented and discussed. The setup is also scrutinised from a practical perspective, where possible improvements, aside from a fibre coupled setup are mentioned. The aim of this section is to discuss the quality of the coupling possible and its practicality for use in the future application.

All the mode coupled traces in this section were obtained for the same fixed angle of the prism and WGMR assembly. The exact value of the angle is unknown, however it was roughly chosen to be slightly larger than $90\,^{\circ}$ with respect to the back face of the prism. Additionally results were only recorded for a single wavelength, $\lambda = 600.2$ nm. Changes in the incident angle could, however, have occurred as a result of the beam position adjustments therefore affecting the modes coupled to.

Using the free beam setup it was possible to achieve mode coupling, the result of which can be seen in figure 26 where the initial fine coupling obtained before any optimisation of the beam was done is shown. The modes are seen as small dips in the signal. As explained in chapter 2, these arise from the interference between the WGMR mode(s) that have been coupled in and subsequently back out of the cavity with the reflected beam in the prism. If complete destructive interference occurs then the dips should reach all the way down to the baseline, indicated by the green line where the detector was blocked. The red line was recorded after the prism had been moved away from the WGMR so that no mode coupling can be seen, i.e. beyond the extent of the evanescent field. It should also be noted that the signal strength is higher than that of the initial mode coupled signal. This is likely to be due to a shift in the beam incident on the detector due to the movement of the prism and therefore a change in the refracted ray incident on the prism and the subsequent TIR angle. This suggests that it should be possible to optimise the signal of the mode coupled beam on the detector.

Figure 26 shows the mode coupled trace after the prism has been moved back to 'touch', indicated by the black line, in comparison to the initial mode coupled trace, indicated by the blue line. It is possible to see an increase in the signal despite the only controlled difference between the two coupling conditions being the prism and WGMR separation. The change in signal strength could therefore be attributed to the aforementioned shift in the beam position through the prism and therefore where it is incident on the detector. Since the prism and WGMR separation has been changed it would seem sensible to assume that this may have influenced the signal level. The prism and WGMR separation is likely to manifest itself in different changes in the mode coupled trace though. As was introduced in the theory in chapter 2, the separation leads to one of three possible outcomes known as; under coupling, critical coupling or over coupling. If under coupling had been the case in the initial mode coupled trace it would be expected that the resonance dips in it, compared to the black line, would occur at the same locations but would be less deep.

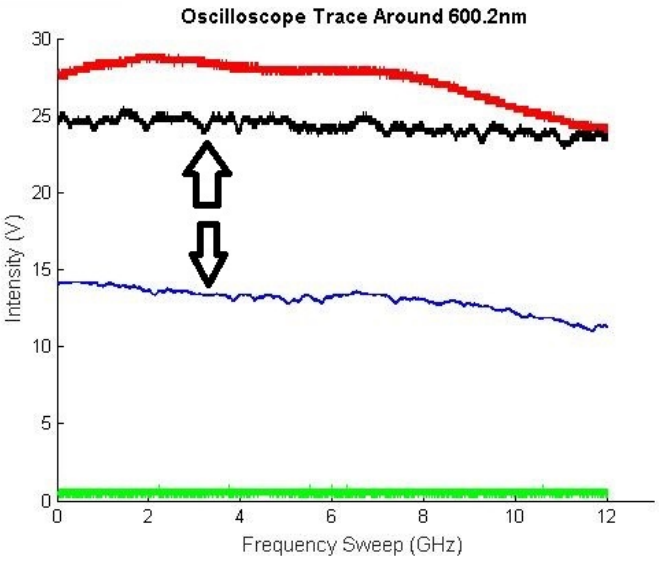

Figure 26: A graph of the mode coupled trace of the Whispering Gallery Mode Resonator around 600.2 nm. The red line indicates a large prism and Whispering Gallery Mode Resonator separation resulting in no coupling. The black and blue lines are mode coupled traces for different prism and Whispering Gallery Mode Resonator separations. The green line indicates the baseline where the detector has been covered.

The arrows on figure 26 indicate a region where modes can be seen in the blue line but not in the black line. If the black line is a more critically coupled version of the blue line then these modes should be visible to at least the same depth as the blue line or deeper. Upon scrutiny of the figure though the mode structures of the two lines do not appear to be the same. This suggests that the angles of the incident TIR beams are not the same and so therefore the phase matching conditions are not the same. Due to the phase matching requirements of each of the modes, the incident TIR angle can be varied in order to couple to different modes. This is normally achieved by rotating the prism and WGMR assembly but it could well result from the differing position of the prism since the attocube and prism are not positioned perpendicularly to the incident beam. An arrow on the figure indicates a region where modes can be seen in the blue line but not in the black line, as an example of the differing mode structure.

Figure 27 shows an array of mode coupled traces for various different positions in optimising the coupling by performing a beam walk with the mirrors. It is possible to see a variation in the signal strength between the different traces. It is also possible to see

some improvement in the resonance dips depths, although it is only slight. One mode, enclosed by a box, was studied as an example and the depth of resonance was found to be; 0.6 V,1.2 V and 1.6 V, for the red, blue and black lines respectively. This indicates that the black line has the most critical coupling of the three. All three mode coupled traces were recorded for the same prism and WGMR separation, only the beam walk and subsequent beam adjustments incident on the detector, were performed.

Despite noticeable improvements in the coupling with beam position adjustments, the coupling efficiency recorded was consistently low. This could be attributed to several different causes such as; the focal spot size and shape being incorrect, the beam alignment being poor with many sources of error and also absorption. Since the absorption is not a parameter that can be removed unless the wavelength is significantly altered as well as the fact that the SHB required the use of a wavelength on a hyperfine level absorption transition of the ions, this can be dealt with later. The crucial first steps to see if the coupling can be improved involve a better aligned beam and also a well shaped focal spot.

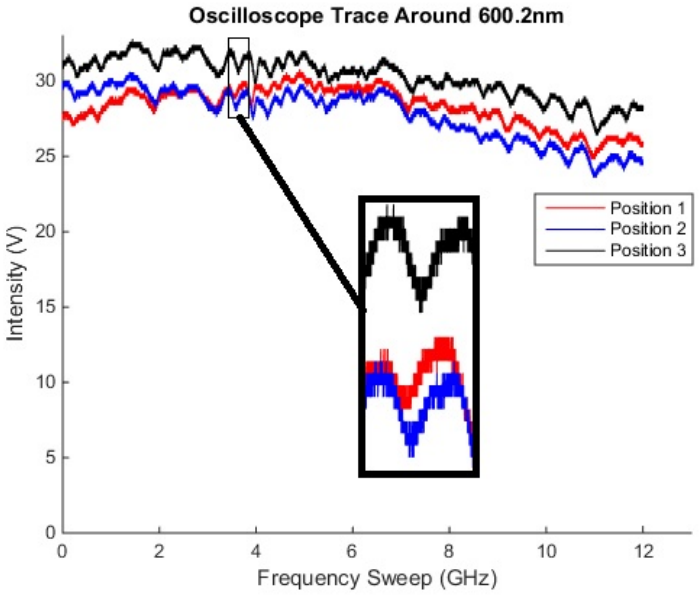

Figure 27: A graph of the mode coupled trace around 600.2 nm for three different beam optimisation settings denoted as position 1, 2 and 3 respectively. A mode has been highlighted by the box where the change in resonance dip depths are compared to show the improvements in coupling achieved at the different beam positions. Position 1 has a depth of 0.6 V, position 2 of 1.2 V and position 3 of 1.6 V showing that the coupling efficiency is best for position 3.

The free beam setup was very difficult to use in terms of assessing changes in the mode coupled trace. In order to make an adjustment in the beam position, both mirrors needed adjusting, followed by the focusing lens and finally the position of the incident beam on the detector, if necessary. During all of these stages it was necessary to recall the original mode coupled trace, before any adjustments were made, and assess whether the new beam position resulted in an improved and poorer trace. When the changes are very slight, since the beam adjustments can only be slight in order to maintain coupling, it is a problematic method. In addition to this, the lens could not be guaranteed to be perpendicular to the beam so that the resultant focal spot was symmetrical. Since the requirement for aperture matching, i.e. complete modal overlap, require the shape and size of the focal spot to match the shape and size of the WGM on the prism's back face, it is critical that the focal spot shape is well controlled. A setup where the lens position

is well aligned with the beam, as well a system where the beam can be translated in the hl$x$,y and z directions in one movement, would greatly simplify the coupling procedure. For this reason a fibre coupled setup was constructed, mimicking the setup described in chapter 3. The following section describes the results obtained from this setup and the improved usability.

6.2 Fibre Coupled Setup

This section presents the results obtained using the fibre coupled setup. In this section mode coupled traces are obtained for a selection of different wavelengths but for the same fixed angle. This angle was, like the free beam setup, unknown but chosen roughly to be slightly larger than 90 °. The results therefore cannot be directly compared with those obtained using the free beam setup since the modes coupled to may not be the same. Additionally, a neutral density filter was used in front of the detector to ensure that the detector was not saturated. For this reason the y-axis of the figures presented here are significantly smaller in scale than the previous section, but this is not indicative of poor mode coupling or low intensity signal from the prism, simply an attenuated signal.

Figure 28 shows the mode coupled trace for $\lambda = 593.8$ nm in blue and the uncoupled (prism moved away from 'touch') trace in red. The mode structure is clearly defined although the resonance dips are still quite shallow. Since the best trace obtained at MPL, figure 28 in chapter 3, had long resonance dips, with the longest stretching over at least 50% of the height, better coupling is expected to be achieved. The coupling performed in chapter 3 was done at $\lambda = 795$ nm which lies outside the absorption range of the ions. Since absorption is likely to contribute the the largest portion of the loss, as discussed in chapter 2, it is useful to identify the significance of the loss due to it.

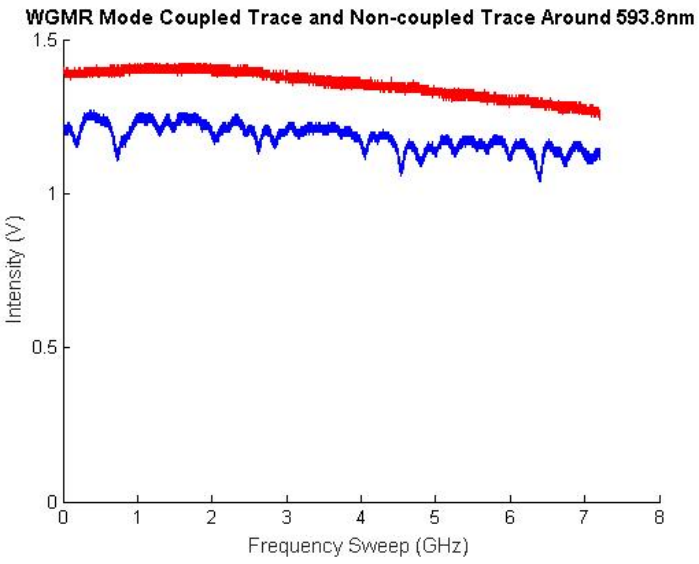

Figure 28: A graph showing the mode coupled trace around 593.6 nm in blue and in red the trace with no mode coupling, achieved when the prism and Whispering Gallery Mode Resonator separation is increased beyond the extent of the evanescent field.

Figure 29 shows the mode coupled traces for different wavelengths but otherwise for all the same conditions, i.e. no adjustment of the incident beam is done. It can be seen that as the wavelength increases from 593.8 nm to 610.4 nm the signal strength reduces and the modes become less clearly defined, to the point that it becomes difficult to dis-

tinguish any modes. The mode coupling reduction could be attributed to absorption for certain wavelengths since, according to figure 47, the absorbance of the ions peaks around 610 nm. This spectrum does not however hold true for all the wavelengths since it would be expected that loss due to absorption would be low and in fact lowest of all the measured wavelengths, at around 605 nm. 606.2 nm does however show possibly the worst coupling where it is in fact very difficult to even determine that there is any coupling since the dips could be mistaken for fluctuations in the laser beam power.

The drop in the signal strength over the various wavelengths presented in figure 29 could be attributed to poor beam alignment incident on the detector. As the wavelength was adjusted the beam path is expected to change thus the angle of the outgoing beam is likely to have changed. This will shift where the beam hits the detector. When the signal dropped the initial check was done by eye to see that the beam still hit the detector in the centre. Fine adjustments could then be made with the mirror if the signal was still low, even when it could be seen in the centre of the detector. It is possible, however, that there was some poor alignment with the detector even after fine adjustment. It would therefore be sensible to optimise the beam position on the detector by checking the full path of the beam from the prism (to ensure no signal has been lost) or by adding additional optics such as a focusing lens. It is critical that all of the beam from the prism is detected. If some of the signal is lost the resulting measurements will be erroneous since some of the contrast resulting from coupling will instead be replaced by an interference of the different out-coupled WGMR modes, [12]. The beam alignment with the detector could be additionally verified as the source of the signal drop by trying different detectors perhaps with larger sensitive regions or by placing the detector closer to the prism output. Of course for the anticipated slow light effect measurements, the detector distance will be restricted and therefore ensuring that the signal is always optimally incident on it at a further distance is more beneficial.

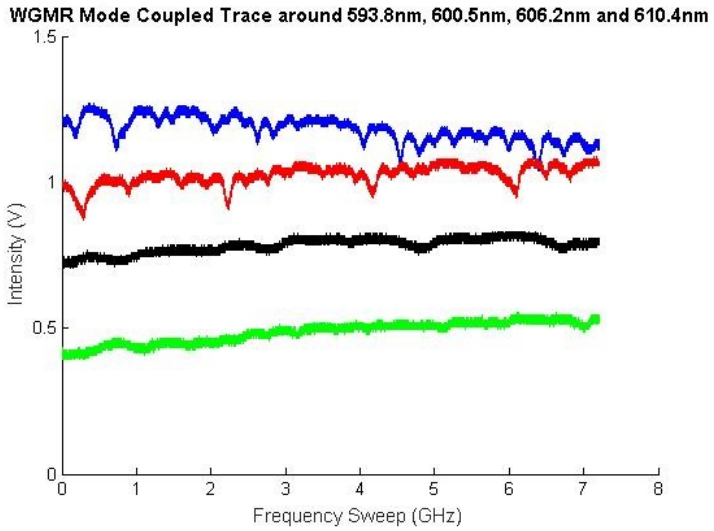

Figure 29: A graph showing the mode coupled trace around four different wavelengths; 593.8 nm (blue), 600.5 nm (red), 606.2 nm(black) and 610.4 nm(green).

Another, larger set of results was recorded for different wavelengths in an attempt to identify a pattern between the absorbance and the coupling. The same trend as before was found. This means that more extensive investigation into optimising the other parameters which effect the coupling should perhaps be performed first. It will then be possible to eliminate any additional effects they may contribute when investigating the

extent to which the absorption effects the coupling loss. Figure 30 illustrates the best and worst mode coupled traces found where the blue line was recorded at $\lambda = 600.5$ nm and the red line at 605.4 nm.

Due to the smaller scan range (9 GHz) of the laser used for the measurements using the fibre coupled setup, a full FSR of the WGMR could not be covered. This in turn, with the addition of small resonance dips, makes it difficult to identify modes which are the same in different traces for different wavelengths. Ideally it should be possible to identify a mode at different wavelengths, with at least two traces containing the same mode, to be able to compare the change in width and depth. This is required in order to be able to comment more accurately on the effect on the total loss and criticality of the coupling experienced by changing certain parameters. Ultimately the aim of these experiments is to create a setup which is easy to operate and can be used in conjunction with the cryostat setup, as well as producing the optimum coupling possible in the chosen wavelength range.

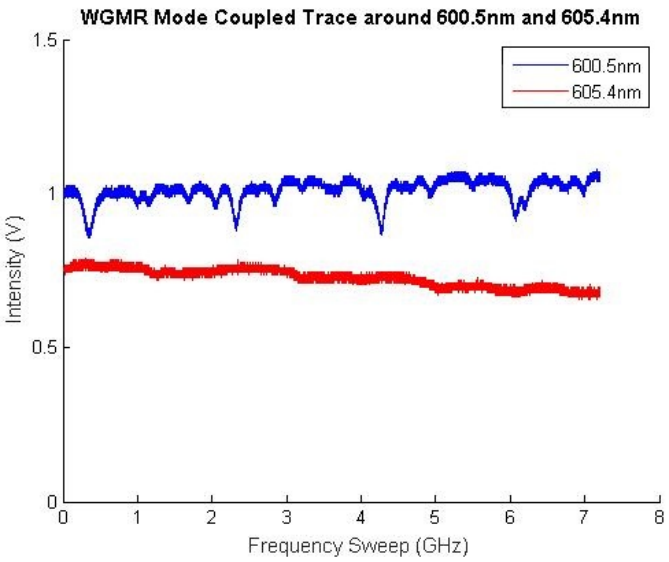

Figure 30: A graph showing the mode coupled trace around 600.5 nm, blue line, and 605.4 nm, red line. These illustrate the best and the worst mode coupling, respectively, achieved when taking a larger set of results for a range of wavelengths between 593.1 nm and 610.4 nm.

6.3 General Discussion

A possible source of poor coupling affecting both of the setups is the focal spot size. An estimated spot size for the fundamental mode of the WGMR is calculated below using the formula for the mode volume as stated in chapter 2. This formula is intended for use in calculating an approximate fundamental mode volume for a spherical WGMR; since a disc shaped WGMR is used in this thesis, the thickness of the disc will act as a limiting factor and therefore the spot size is subject to error.

$$V_{eff} = 3.4\pi^{\frac{3}{2}} \left(\frac{600 \times 10^{-9}}{2\pi 1.8} \right)^3 39018^{\frac{11}{6}} \sqrt{1} \text{ cm}^3 = 7.389 \times 10^{-7} \text{ cm}^3 \tag{23}$$

$$A = \frac{V_{eff}}{2\pi R} = \frac{7.389 \times 10^{-13}}{2\pi 0.00207} \text{ cm}^3 \tag{24}$$

$$r = \sqrt{\frac{V_{eff}}{2\pi^2 R}} = 4.25 \times 10^{-6} \text{ m} \tag{25}$$

So the spot diameter is 8.51×10^{-6} m (≈ 9 µm).

The significance of using the appropriate spot size is to avoid parasitic mode coupling. This means the coupling to additional modes than the one(s) desired. There is also an additional effect which can result from coupling to multiple modes called intermodal mixing. This is when the different modes overlap with each other and interact. This limits the maximum possible coupling since the desired mode emits into the other modes, [12]. Intermodal mixing leads to non-linear behaviour, [17], which is not desirable in the future slow light effect experiment. The spot size used in the fibre coupled setup was significantly smaller than the one in the free beam setup. Since the smallest focal spot was still greater than the above calculated value, both experiments are equally susceptible to parasitic mode coupling. Due to the larger area of the incident spot size compared to the desired spot size for one mode, the evanescent field generated will be wider. If the spacing between the prism and WGMR in the extended regions is sufficiently small so that the evanescent field has not decayed then propagative waves will be possible in the WGMR in the region of the extended field. Using a focal lens with a shorter focal length, or broadening the collimated laser beam incident on the lens, could be used to generate a smaller spot size. The latter option is more useful to try since the setup should ultimately be usable for the slow light effect measurements. The focal length needs to be greater than 110 mm, the length from the outer cryostat window to the centre of the chamber.

Mode coupling in both the coarse and fine coupling stages was accompanied by a distinct glow (fluorescence) of the WGMR, as shown in figure 31. Although this made it obvious when the mode was being coupled to, it will be less useful due to substantially reduced visibility of the WGMR in the cryostat setup.

Figure 31: A photograph of the Whispering Gallery Mode Resonator with light coupled into it. The red 'glow' shows the florescence from the Praseodymium ions, due to the interaction with incoupled light.

The fibre coupled setup provided an improved system for alignment in terms of ease of use. However, it is still not entirely possible to determine whether the coupling efficiency, ideality and criticality, were significantly or at all improved as a direct result of the fibre coupled setup. It is however the better choice of the two tested setups to proceed with to optimise the coupling. The beam from the fibre setup appeared not to be entirely parallel with to the optical table as the beam out of the prism was often clipped by the prism mount plate. This needs to be rectified and would be best done with the use of an additional translational stage which can control the tilt of

the beam in both the vertical and horizontal planes. This is suggested since the prism coupling setup has a number of degrees of freedom due to the placement of the prism, the placement of the WGMR and the subsequent orientation of the beam. Allowing the beam to be manipulated in as many directions as possible allows as many of the different degrees of freedom to be optimised by adjusting it.

7 Conclusion and Outlook

Slow light effects, resulting from the creation of slow light structures from SHB, have been found to be useful in many applications. Similarly WGMRs, although young in terms of research compared to conventional resonators, have shown very useful unique properties for use across many fields leading to more interest in them. The aim of this thesis is to combine these two fields of study and to lay the foundations for an experiment which will ultimately investigate slow light effects in WGMRs.

Due to the no previous WGMR studies having been performed in the QI group in Lund, the thesis began by presenting an overview of the main areas of the theory required in the anticipated experiment. Practical experience was then gained by visiting a group based in MPL, who have well established research using WGMRs for various applications such as bio-sensing. The knowledge gained was then applied to both the design of a proposed holder to be placed into the cryostat as well as creating and using an experimental setup to perform mode coupling.

The results show that coupling is possible using both a crude experimental regime (free beam setup) as well as a more refined setup using a fibre coupled beam. It was found, however, that the control over the manipulation of the beam and subsequently the focal spot position, was better using the fibre coupled setup. It allowed a control over the movement in the three axes, x-y-z, where the effects could be clearly and quickly monitored by changes in the oscilloscope mode trace.
By comparing the rough mode coupling results obtained in Germany to those found here, it can be seen that the efficiency of coupling to this WGMR can be better than those obtained in the free beam and fibre coupled setups. Since the wavelengths use for coupling in the two cases, Germany and Lund, were not the same, the decrease in coupling could be attributed to loss due to absorption of the Pr^{3+} ions. The fibre coupled setup was therefore used to obtain results at various wavelengths in order to establish if this theory is correct and therefore maximum possible coupling achievable. A change in the mode coupling was seen for the various wavelengths; however it did not follow the expected variation according to the absorbance spectrum of the ions. When the mode coupled traces deteriorated, for wavelengths around 606 nm and 610 nm, the mode structure became so unclear that it was not possible to determine a mode in them to use to compare the depth and width with the same mode for a different initial wavelength scan.
The low efficiency coupling was also attributed to potentially poor modal overlap and parasitic mode coupling. These arise from the size and shape of the focal spot used. The focal spot size for the fundamental mode of the WGMR was estimated and compared to the spot sizes used in the two setups. It was found that both of the spot sizes were too large and therefore better mode coupling should be possible if a smaller, size and shaped matched focal spot is chosen instead. It would therefore be advisable to perform mode coupling with a variety of different lenses such that a selection of focal spot sizes close to the approximated one are tested. It would also be interesting to look at coupling for spot sizes smaller than the approximated one, if possible.
As mentioned above, the shape of the focal spot is also important. When the incident Gaussian beam meets the back face of the prism, it becomes elongated in shape. If the

WGMR has equal radii of curvature, i.e. spherical, then this elongated shape will not match the WGMR mode shape, which would be symmetrical. The use of astigmatic optics could then be implemented to shape the spot in order to match it with the WGMR mode shape. Two things would then need to be known; the incident beam spot shape of the back face of the prism and the WGMR mode shape at the 'touch' point. Calculations can be done to check both and then simulations for the optics required to manipulate the spot shape could be performed. Since the WGMR used here is a disc with a curved (axial) edge, its shape is already defined, meaning that manipulation of the beam spot shape is the only parameter to be changed. Of course other resonators can be fabricated where they are shaped to match the beam spot. Since the WGMR is a disc, it can be assumed that its two radii of curvature are not equal ($R \neq r$), such that an elongated mode spot shape would result. In order to determine the mode spot shape it is necessary to measure r. This can be done by measuring the Newton rings between the WGMR rim and a glass slide under a microscope. The vertical radius of curvature, r, can then be determined by solving the relationship between R and r given in figure 32, where the ratio of the lengths from the centre of the interference pattern out to a selected number of rings are compared.

Additional loss mechanisms, aside from the absorption and modal overlap mismatch, arise from surface scattering and radiative losses. The radiative loss, for large WGMRs, is small but it is possible to calculate the estimated contribution from equation (17), given in chapter 2. The surface scattering, however, can contribute significantly to the loss. It would therefore be beneficial to verify the estimated surface scattering contribution by doing an Atomic Force Microscopy measurement of the surface of the outer rim of the WGMR. It is therefore possible to use equation (16) to determine the surface scattering loss.

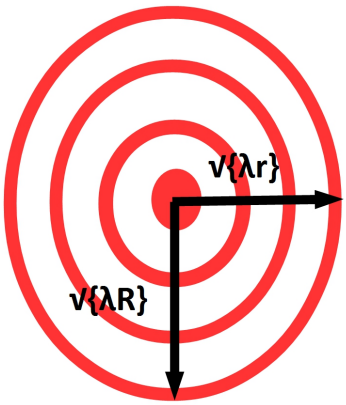

Figure 32: An illustration of the Newton Rings pattern seen at the boundary between the Whispering Gallery Mode Resonator rim and a flat glass plate. The annotations describe the ratio between the radial radius of curvature (R) and the axial radius of curvature (r) such that it is possible to determine r if λ and R are known. This measurement can be performed using a microscope of 20x magnification.

By implementing the above suggested changes and by determining the extent of the various loss mechanisms present in the coupling, it should be possible to optimise the setup so that coupling can be performed close to the maximum theoretical efficiency. When this has been achieved the mode trace should produce the longest and narrowest resonance dips possible for the optimal experimental conditions. The Q-factor can then be measured from the experimental data and compared to theoretical values. At this stage the coupling efficiency is quite low and there are several loss mechanisms that can be assumed to not have been optimised for. As a result any calculation of the Q-factor from the existing results would not give an accurate representation of the WGMRs Q-factor for the chosen wavelength range and operating temperature. It is, however, critical to calculate the

Q-factor accurately since the aim of the planned experiment to investigate slow light effects in WGMRs aims to see if improvements in the Q-factor can result. If there are errors in the value for the determined Q-factor before and as a result of slow light effects then it will not be possible to draw any accurate conclusions since it will be unclear if the effects are due to slow light effects.

If the anticipated improvement in the Q-factor is achieved from slow light effects then there would be applications for the WGMRs under this regime. Since the resonance linewidths would be narrowed the frequency resolution of the WGMR would be improved with applications in laser stabilisation. Experiments involving the increase of the Purcell effect could also benefit since a small mode volume, characteristic of WGMRs, and the anticipated increase in the Q-factor, would enhance the Purcell effect.

References

[1] American Physical Society, Physics, *Focus: Slow Light for the Rest of Us*, `http://physics.aps.org/story/v3/st37`,Phys. Rev. Focus 3, 37, June 29, (1999)

[2] Nilsson M., *Coherent Interactions in Rare-Earth-Ion-Doped-Crystals for Applications in Quantum Information Science*, Doctoral Thesis, Atomic Physics Division, Dept. of Physics, Lund Institute of Technology, ISBN:91-628-6377-0, (2004).

[3] Şahin Kaya Özdemir, Jiangang Zhu, Lina He, and Lan Yang, *Estimation of Purcell factor from mode-splitting spectra in an optical microcavity*, Phys. Rev. A 83, 033817, 18 March, (2011)

[4] T. J. Kippenberg, A. L. Tchebotareva, J. Kalkman, A. Polman, and K. J. Vahala, *Purcell-Factor-Enhanced Scattering from Si Nanocrystals in an Optical Microcavity*,Phys. Rev. Lett. 103, 027406, 10 July, (2009)

[5] Rippe L., *Quantum Computing With Naturally Trapped Sub-Nanomere-Spaced Ions*, Doctoral Thesis, Atomic Physics Division, Dept. of Physics, Lund Institute of Technology, ISBN:91-628-6907-8, (2006).

[6] Walther A., *Coherent Processes in Rare-Earth-Ion-Doped Solids*, Doctoral Thesis, Atomic Physics Division, Dept. of Physics, Lund Institute of Technology, ISBN:978-91-628-7718-7, (2009).

[7] Ekelund R. *Retrieval of cavity embedded absorption spectrum for quantum memory applications*, Master's Thesis, Quantum Information Group, Lund University, Feb 24, (2014)

[8] Gonzalez-Herraez M.,Esteban O., Naranjo F.B. and Thevenaz L. *How to play with the spectral sensitivity of interferometers using slow light concepts - and how to do it practically* SPIE Vol. 6619, 661937, doi:10.1117/12.738653, (2007)

[9] de Fornel, F., *Evanescent Waves: From Newtonian Optics to Atomic Optics*, Springer Series in Optical Sciences, Vol. 73, Springer-Verlag Berlin Heidelberg, ISBN:978-3-540-65845-0, (2001)

[10] He, L., *Whispering Gallery Mode Microresonators for Lasing and Single Nanoparticle Detection*, All Theses and Dissertations (ETDs), Paper 697, `http://openscholarship.wustl.edu/etd/697`, (2012)

[11] Sprenger B., *Stabilizing lasers using Whispering gallery mode resonators*, Doctoral Thesis, Friedrich-Alexander Universität Erlangen-Nürnberg, (2010)

[12] Maleki L., Ilchenko V.S., Savchenkov A.A. and Matsko A.B., *Crystalline Whispering Gallery Mode Resonators in Optics and Photonics*, Practical Applications of Microresonators in Optics and Photonics, Taylor and Francis Group, LLC, (2009)

[13] Krupka J., Cwikla A., Mrozowski M., Clarke R.N., Tobar M.E.,*High Q-factor microwave Fabry-Perot resonator with distributed Bragg reflectors*, Ultrasonics, Ferroelectrics, and Frequency Control, IEEE Transactions on, vol. 52, pages 1443-1451, Sept., (2005)

[14] Schwefel H.G.L., *Whispering Gallery Mode Resonators*, Institute for Optics, Information and Photonics, University of Erlangen-Nuremberg, Mar. 25th, (2014) - currently unpublished

[15] Gribbin D.J., *Development of Whispering Gallery Mode Resonators in Lithium Niobate*, Bachelor's Thesis, College of William and Mary in Virginia, `http://physics.wm.edu/Seniorthesis/SeniorThesis2011/Gribbin%20David.pdf`, May, (2011)

[16] Attocube Systems AG, Koeniginstrasse 11a, 80539 Muenchen (Germany), `http://www.attocube.com`

[17] Shi T. and Fan S., *Two-photon transport through a waveguide coupling to a whispering-gallery resonator containing an atom and photon-blockade effect*, American Physical Society, Phys. Rev. A, vol. 87, issue 6, 063818, doi: 10.1103/PhysRevA.87.063818, June 13th, (2013)

[18] Righini G., Dumeige Y., Féron P., Ferrari M., Nunzi C., Gualtiero, Ristic, Davor and Soria S.*Whispering gallery mode microresonators : Fundamentals and applications*,Rivista del Nuovo Cimento,Società Italiana di Fisica, Vol. 34, doi: 10.1393/ncr/i2011-10067-2, Jul, (2011)

[19] Saleh B.E.A, Teich M.C., *Fundamentals of Photonics*, Wiley Series in Pure and Applied Optics, 2nd Edition ISBN:978-0-471-35832-9, (2007)

8 Appendix

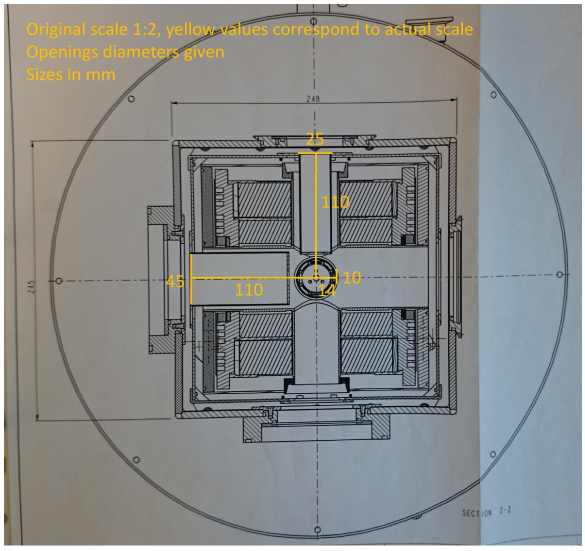

Figure 33: A schematic of the cryostat with some dimensions (in millimetres) marked. This figure is taken from the manual for the cryostat.

Code for calculating the internal prism angles. The refractive indices of diamond and liquid helium are used in order to determine the angle, α , for which the 'angle', between in the incident and reflected beams, is 90°.

```
nd=2.419;
nh=1.025;

for beta = 1:0.2:90
theta = asind((nh*sind(beta))/nd);
alpha=2*(180-(90-theta)-48); %from calculated theta and given beta
angle = alpha+(2*beta); %want angle to equal 90degrees
M=[beta theta alpha angle];
disp(M)
end
```

attoMOTION
Piezo-based Nanopositioners

ANPx51

compact, open loop, linear, horizontal stepper positioner

Technical Specifications

Technology	
travel mechanism	inertial piezo drive

Size and Dimensions	
footprint; height	15 x 15; 9.2 mm
maximum size	15 x 18; 9.2 mm
weight	7 g

Coarse Positioning Mode	@ 300 K	@ 4 K
input voltage range	0 .. 60 V	0 .. 60 V
typical actuator capacitance	1.05 µF	0.15 µF
travel range (step mode)	3 mm	3 mm
typical minimum step size	50 nm	10 nm
maximum drive velocity	≈ 1 mm/s	

Fine Positioning Mode	@ 300 K	@ 4 K
input voltage range	0 .. 100 V	0 .. 150 V
fine positiong range	0 .. 5 µm	0 .. 0.8 µm
fine positioning resolution	sub-nm	sub-nm

Materials (non-magnetic)	
positioner body	titanium (upgrade option: beryllium copper)
actuator	PZT ceramics
connecting wires	insulated twisted pair, copper

Load (@ ambient conditions)	mounting orientation: axis horizontal
maximum load	0.25 N (25 g)
maximum dynamic force along the axis	1 N

Mounting	
from the top	2 through holes dia 1.7 mm, cntrbr. f. M1.6
from the bottom	2 threads M2 x 2.5 mm
load on top	4 threads M1.6 x 2.5 mm

Article Numbers	
/RT Version	1002223
/HV Version	1002219
/UHV Version	1002224
/LT Version	1002220
/LT/HV Version	1002221
/LT/UHV Version	1002222

Compatibility with Electronics	
ANC300 piezo positioning controller	ANM150, ANM300

Working Conditions	
mounting orientation	axis horizontal
magnetic field range	0 .. 31 T
temperature range (/RT, /HV, /UHV)	0 ..100 °C
temperature range (/LT, /LT/HV, /LT/UHV)	10 mK .. 373 K
max. bake out temperature (/UHV, /LT/UHV)	150 °C
minimum pressure (/RT, /LT)	1E-4 mbar
minimum pressure (/HV, /LT/HV)	1E-8 mbar
minimum pressure (/UHV, /LT/UHV)	5E-11 mbar

Accuracy of Movement	
repeatability of step sizes	typically 5 % over full range
forward / backward step asymmetry	typically 5 %

Connectors and Feedthroughs	/RT, /LT Versions	all /HV, /UHV Versions
connector type	2-pole pin plug, ø 0.5 mm, d = 2 mm, 30 cm cable with connector	2-pole pin plug (PEEK), ø 0.5 mm, d = 2 mm, 30 cm cable with connector
electrical feedthrough solution	VFT/LT	VFT/HV, VFT/UHV

Technical Drawings

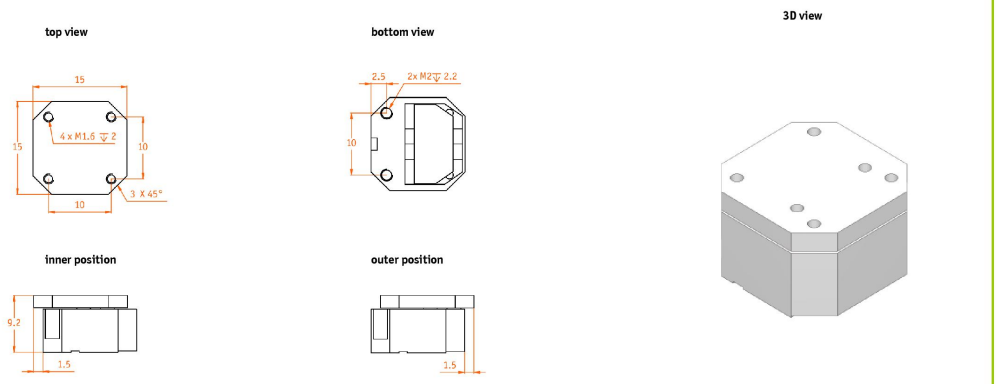

attocube
pioneers of precision

Figure 34: Technical details of the translational attocube (ANPx51), with feedback, taken from the attocube company website [16]

attoMOTION
Piezo-based Nanopositioners

ANPx51/RES

compact, closed loop, linear, horizontal stepper positioner with resistive encoder

Technical Specifications

Technology	
travel mechanism	inertial piezo drive

Size and Dimensions	
footprint; height	15 x 18; 9.2 mm
maximum size	18 x 18; 9.2 mm
weight	7.2 g

Coarse Positioning Mode	@ 300 K	@ 4 K
input voltage range	0 .. 60 V	0 .. 60 V
typical actuator capacitance	1.05 µF	0.15 µF
travel range (step mode)	3 mm	3 mm
typical minimum step size	50 nm	10 nm
maximum drive velocity	≈ 1 mm/s	

Fine Positioning Mode	@ 300 K	@ 4 K
input voltage range	0 .. 100 V	0 .. 150 V
fine positiong range	0 .. 5 µm	0 .. 0.8 µm
fine positioning resolution	sub-nm	sub-nm

Materials (non-magnetic)	
positioner body	titanium (upgrade option: beryllium copper)
actuator	PZT ceramics
connecting wires	insulated twisted pair, copper

Load (@ ambient conditions)	mounting orientation: axis horizontal
Load (@ ambient conditions)	0.25 N (25 g)
maximum dynamic force along the axis	1 N

Mounting	
from the top	2 through holes dia 1.7 mm, cntrbr. f. M1.6
from the bottom	2 threads M2 x 2.5 mm
load on top	4 threads M1.6 x 2.5 mm

Article Numbers	
/RT Version	1003261
/HV Version	1003263
/UHV Version	1003264
/LT Version	1003262
/LT/HV Version	1003265
/LT/UHV Version	1003266

Compatibility with Electronics	
ANC350 piezo positioning controller	ANC350/RES

Working Conditions	
mounting orientation	axis horizontal
magnetic field range	0 .. 31 T
temperature range (/LT, /LT/HV, /LT/UHV)	10 mK .. 373 K
max. bake out temperature (/UHV, /LT/UHV)	150 °C
minimum pressure (/RT, /LT)	1E-4 mbar
minimum pressure (/HV, /LT/HV)	1E-8 mbar
minimum pressure (/UHV, /LT/UHV)	5E-11 mbar

Position Encoder	
readout mechanism	resistive sensor
sensor power (when measuring)	1 µW .. 1 mW
encoded travel range	full travel
sensor resolution	≈ 200 nm
repeatability	1..2 µm
linearity (over full travel)	< 1%
absolute accuracy	typically < 1.5 % of travel range

Connectors and Feedthroughs	/RT, /LT Versions	all /HV, /UHV Versions
connector type	2-pole pin plug, ø 0.5 mm, d = 2 mm, 30 cm cable with connector	2-pole pin plug (PEEK), ø 0.5 mm, d = 2 mm, 30 cm cable with connector
encoder connector	additional 3-pole plug	additional 3-pole plug (PEEK)
electrical feedthrough solution	VFT/LT	VFT/HV, VFT/UHV

Technical Drawings

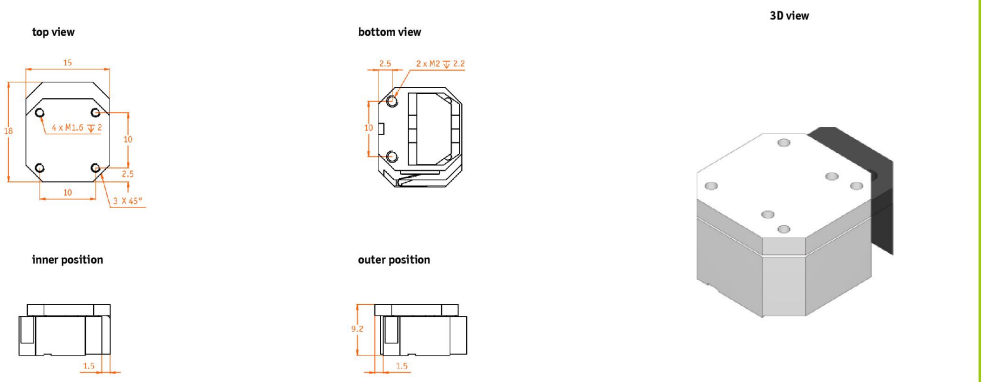

attocube
pioneers of precision

Figure 35: Technical details of the translational attocube (ANPx51/RES), with feedback, taken from the attocube company website[16]

attoMOTION
Piezo-based Nanopositioners

ANR51/RES

compact, closed loop, rotary stepper positioner with vertical rotation axis and resisistive encoder

Technical Specifications

Technology	
travel mechanism	inertial piezo drive

Size and Dimensions	
footprint; height	15 x 15 (Ø 20); 9.5 mm
weight	10 g
through hole in the middle of the axis	Ø 1.5 mm

Coarse Positioning Mode	@ 300 K	@ 4 K
input voltage range	0 .. 60 V	0 .. 60 V
typical actuator capacitance	1.9 µF	0.4 µF
travel range (step mode)	360° endless, both directions	
typical minimum step size	1 m°	0.5 m°
maximum drive velocity	≈ 10 °/s	

Fine Positioning Mode	@ 300 K	@ 4 K
input voltage range	0 .. 60 V	0 .. 150 V
fine positiong range	0 .. 40 m°	0 .. 6 m°
fine positioning resolution	µ°	µ°

Materials (non-magnetic)	
positioner body	titanium (upgrade option: beryllium copper)
actuator	PZT ceramics
connecting wires	insulated twisted pair, copper

Load (@ ambient conditions)	mounting orientation: axis vertical
maximum load	0.3 N (30 g)
maximum dynamic torque around axis	0.2 Ncm

Mounting	
from the bottom	2 threads M2 x 2.3 mm
load on top	2 threads M1.6 x 1 mm

Article Numbers	
/RT Version	1003291
/HV Version	1003293
/UHV Version	1003294
/LT Version	1003292
/LT/HV Version	1003295
/LT/UHV Version	1003296

Compatibility with Electronics	
ANC350 piezo positioning controller	ANC350/RES

Working Conditions	
mounting orientation	axis vertical
magnetic field range	0 .. 31 T
temperature range (/LT, /LT/HV, /LT/UHV)	10 mK .. 373 K
max. bake out temperature (/UHV, /LT/UHV)	150 °C
minimum pressure (/RT, /LT)	1E-4 mbar
minimum pressure (/HV, /LT/HV)	1E-8 mbar
minimum pressure (/UHV, /LT/UHV)	5E-11 mbar

Accuracy of Movement	
wobble	± 1 mrad

Position Encoder	
readout mechanism	resistive sensor
sensor power (when measuring)	1 µW .. 1 mW
encoded travel range	315°
sensor resolution	≈ 6 m°
repeatability	≈ 50 m°
linearity (over full travel)	< 1%
absolute accuracy	typically < 1 % of travel range

Connectors and Feedthroughs	/RT, /LT Versions	all /HV, /UHV Versions
connector type	2-pole pin plug, ø 0.5 mm, d = 2 mm, 30 cm cable with connector	2-pole pin plug (PEEK), ø 0.5 mm, d = 2 mm, 30 cm cable with connector
encoder connector	additional 3-pole plug	additional 3-pole plug (PEEK)
electrical feedthrough solution	VFT/LT	VFT/HV, VFT/UHV

Technical Drawings

top view

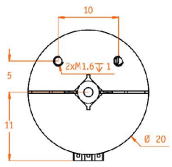

bottom view

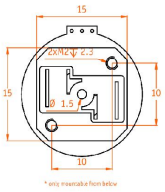

3D view

side view

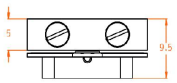

attocube
pioneers of precision

Figure 36: Technical details of the rotating attocube (ANR51/RES), with feedback, taken from the attocube company website [16]

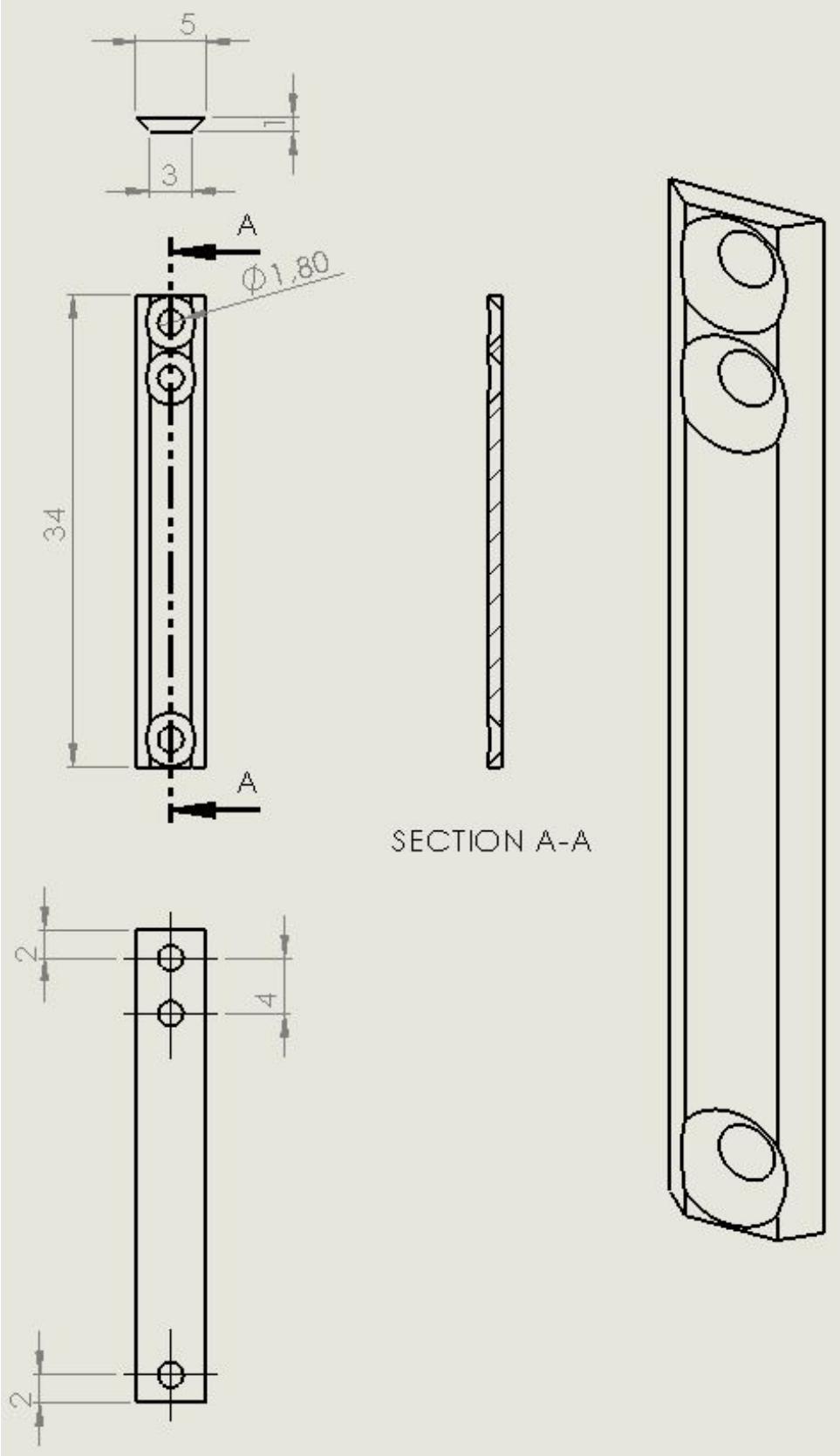

Figure 37: Solidworks model drawing of the rear inner frame bar of the cryostat holder

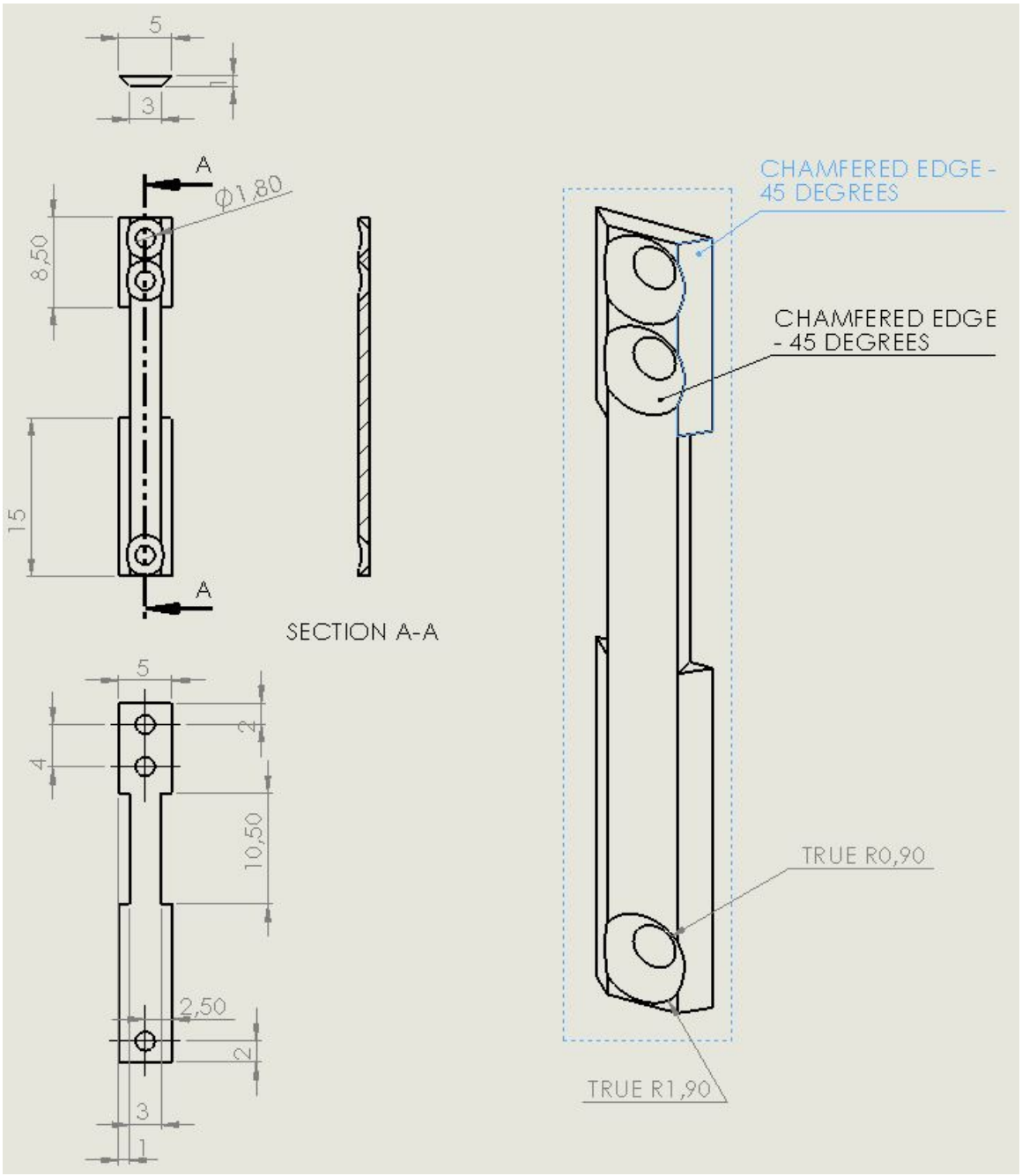

Figure 38: Solidworks model drawing of the central (in relation to the incoming beam) inner frame bar of the cryostat holder

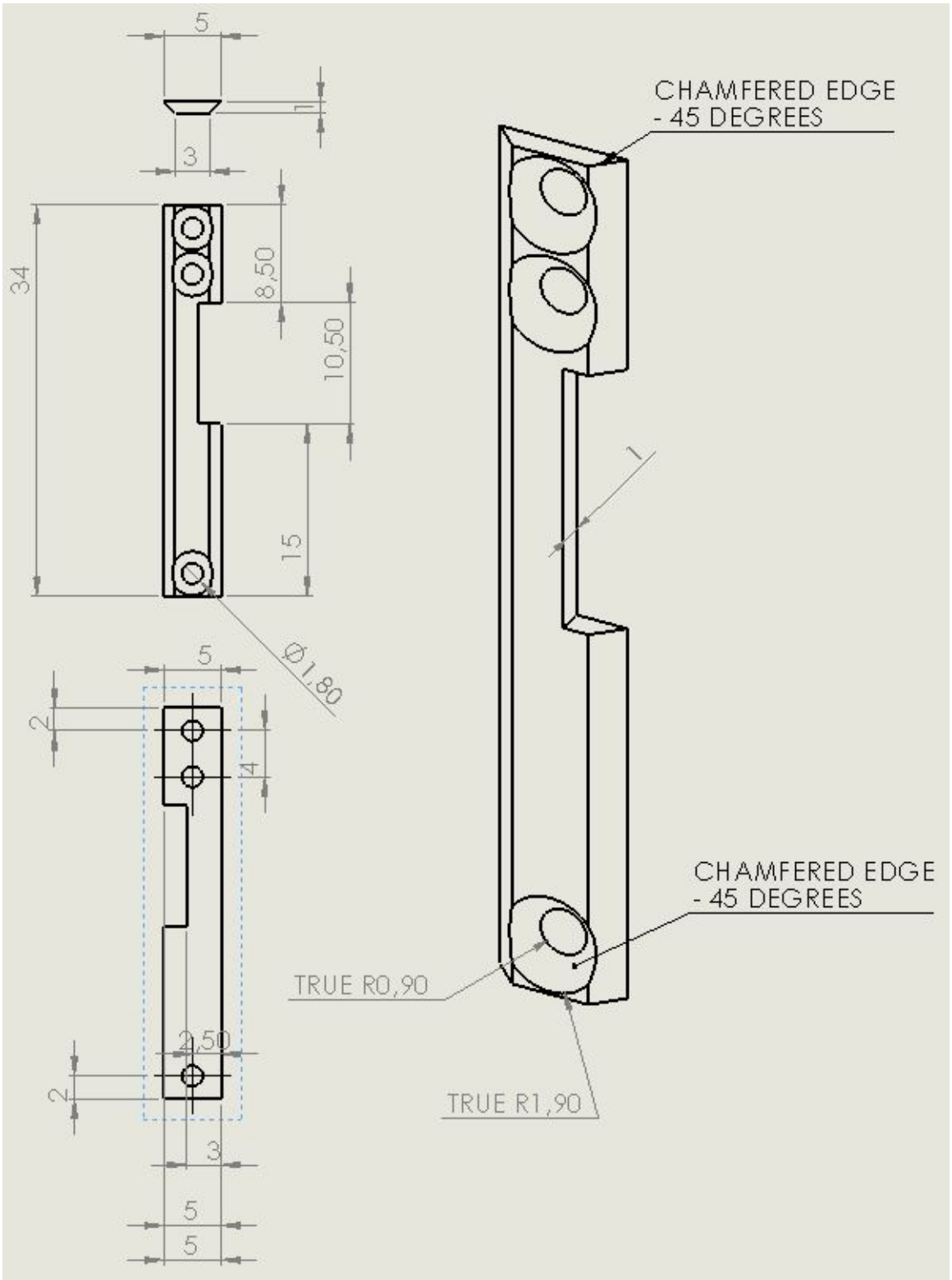

Figure 39: Solidworks model drawing of the left-hand (in relation to the incoming beam), inner frame bar of the cryostat holder

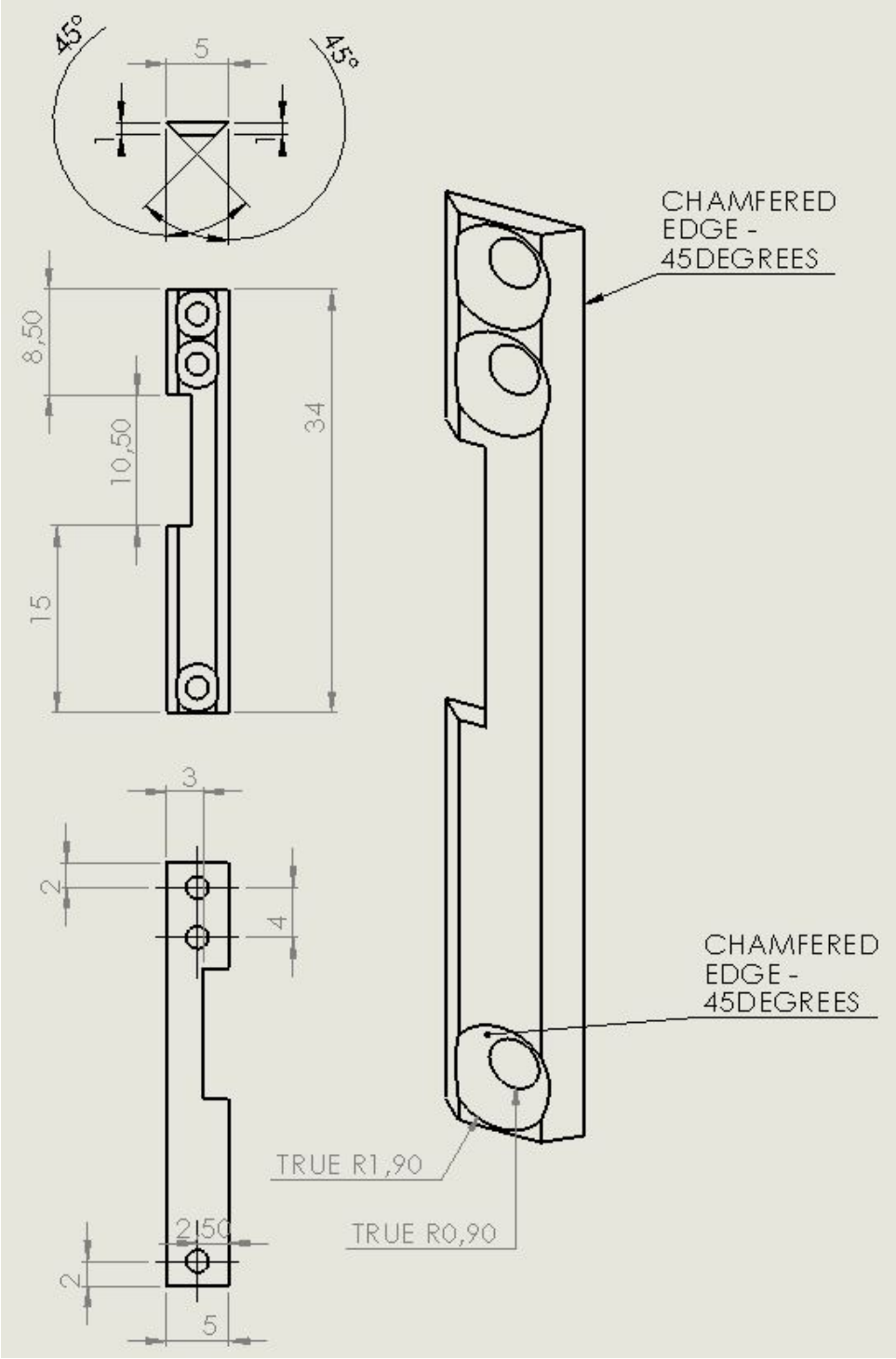

Figure 40: Solidworks model drawing of the right-hand (in relation to the incoming beam), inner frame bar of the cryostat holder

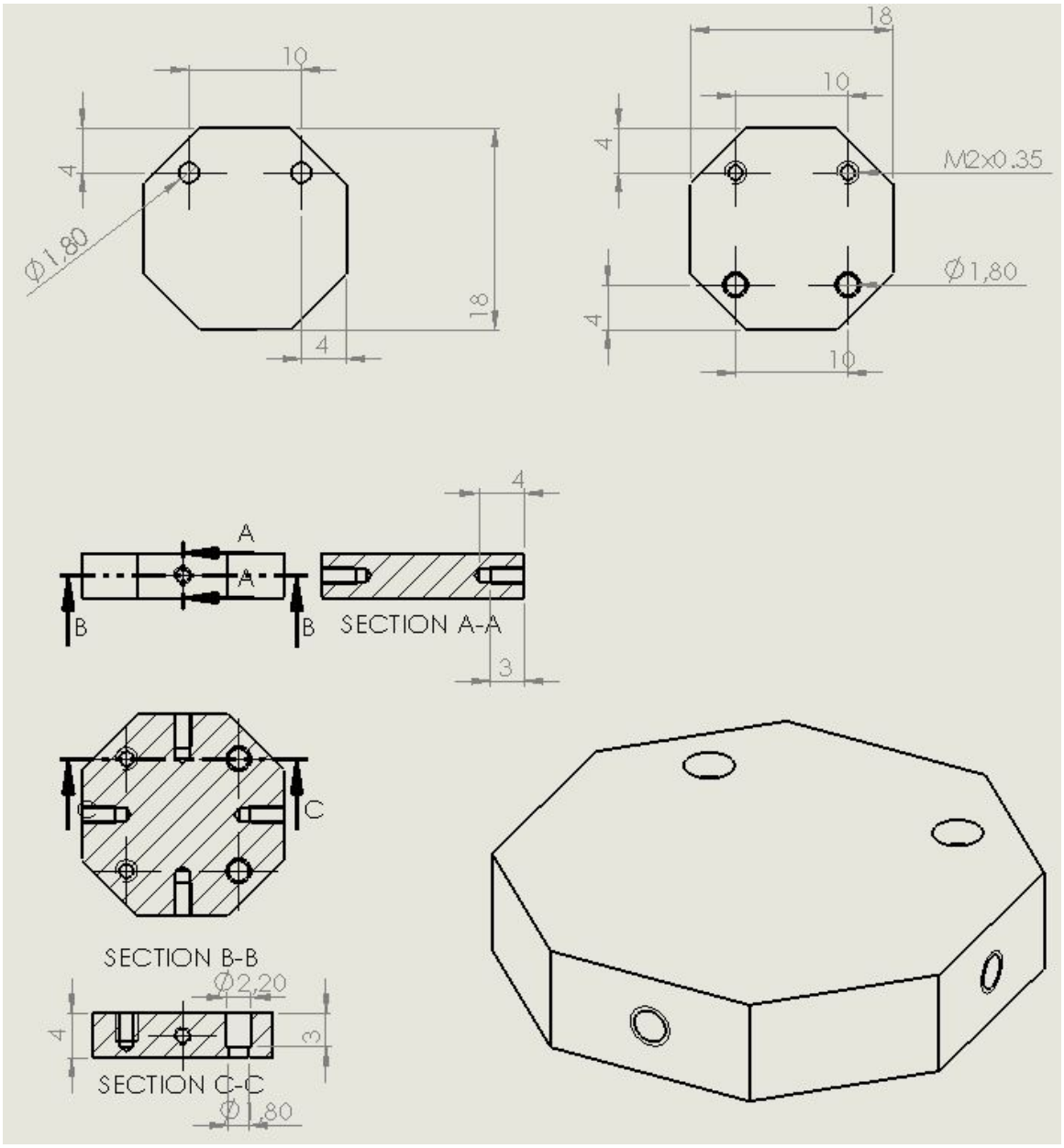

Figure 41: Solidworks model drawing of the base plate of the inner frame of the cryostat holder

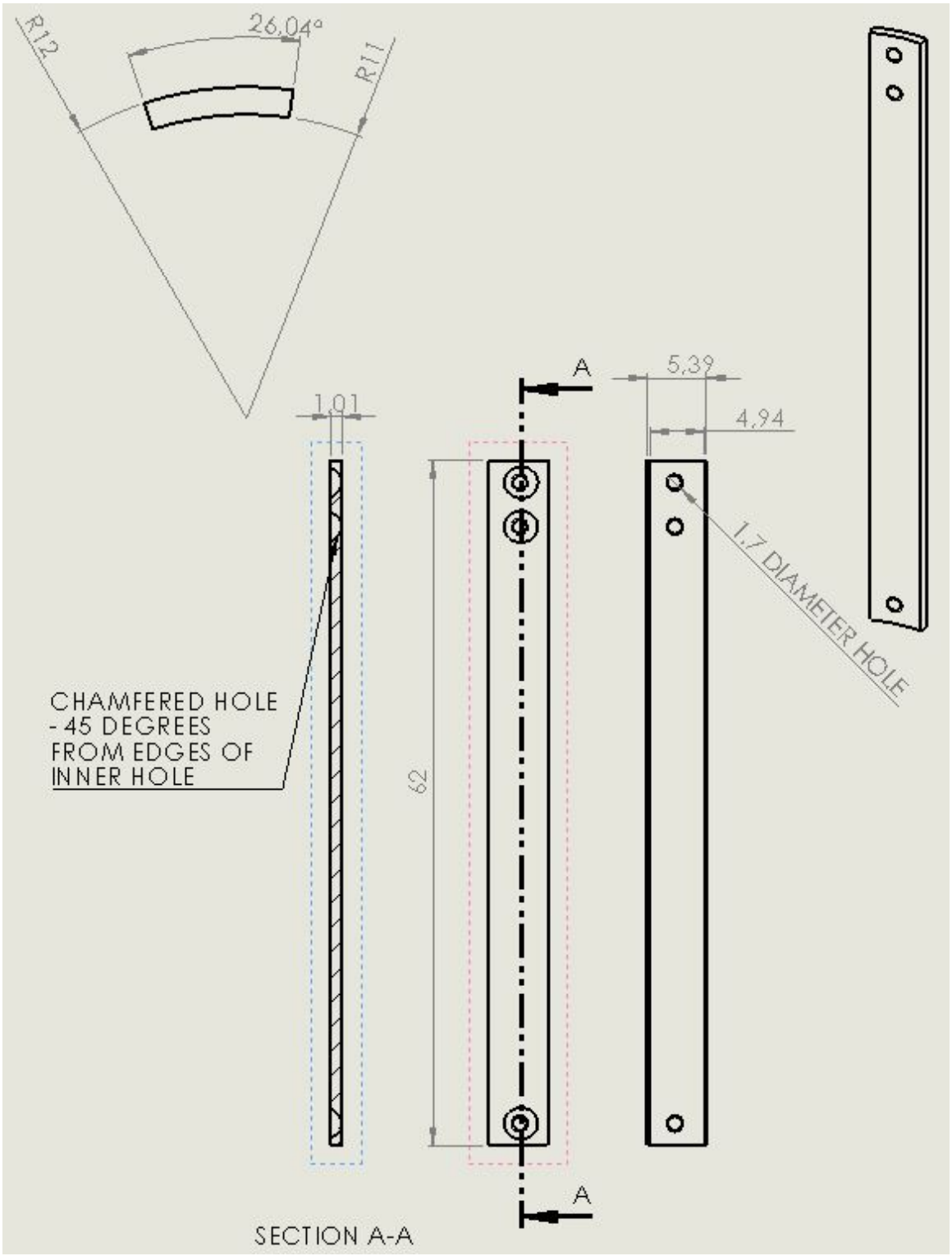

Figure 42: Solidworks model drawing of the outer frame bar(s) of the cryostat holder

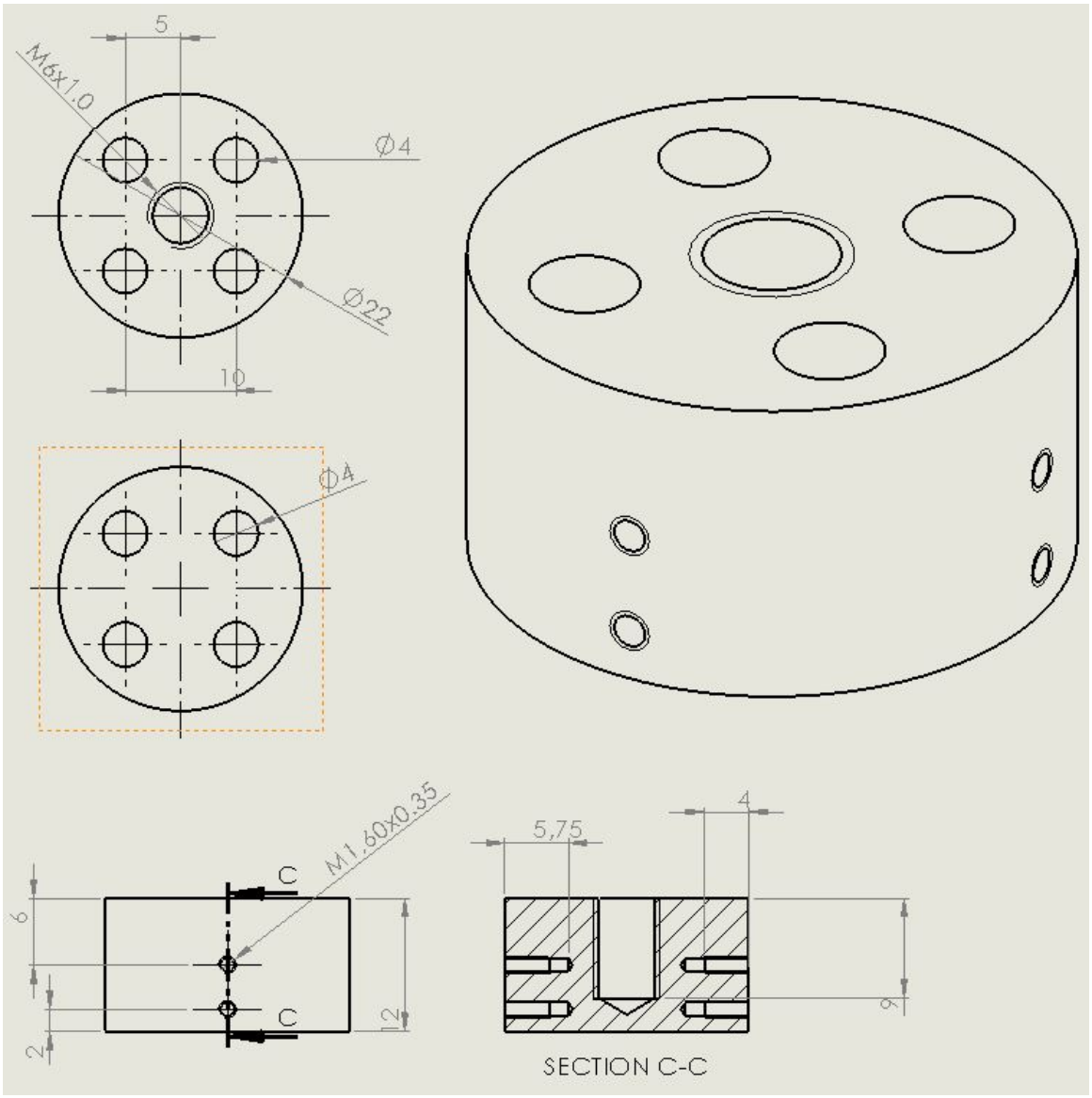

Figure 43: Solidworks model drawing of the upper plate of the outer frame of the cryostat holder

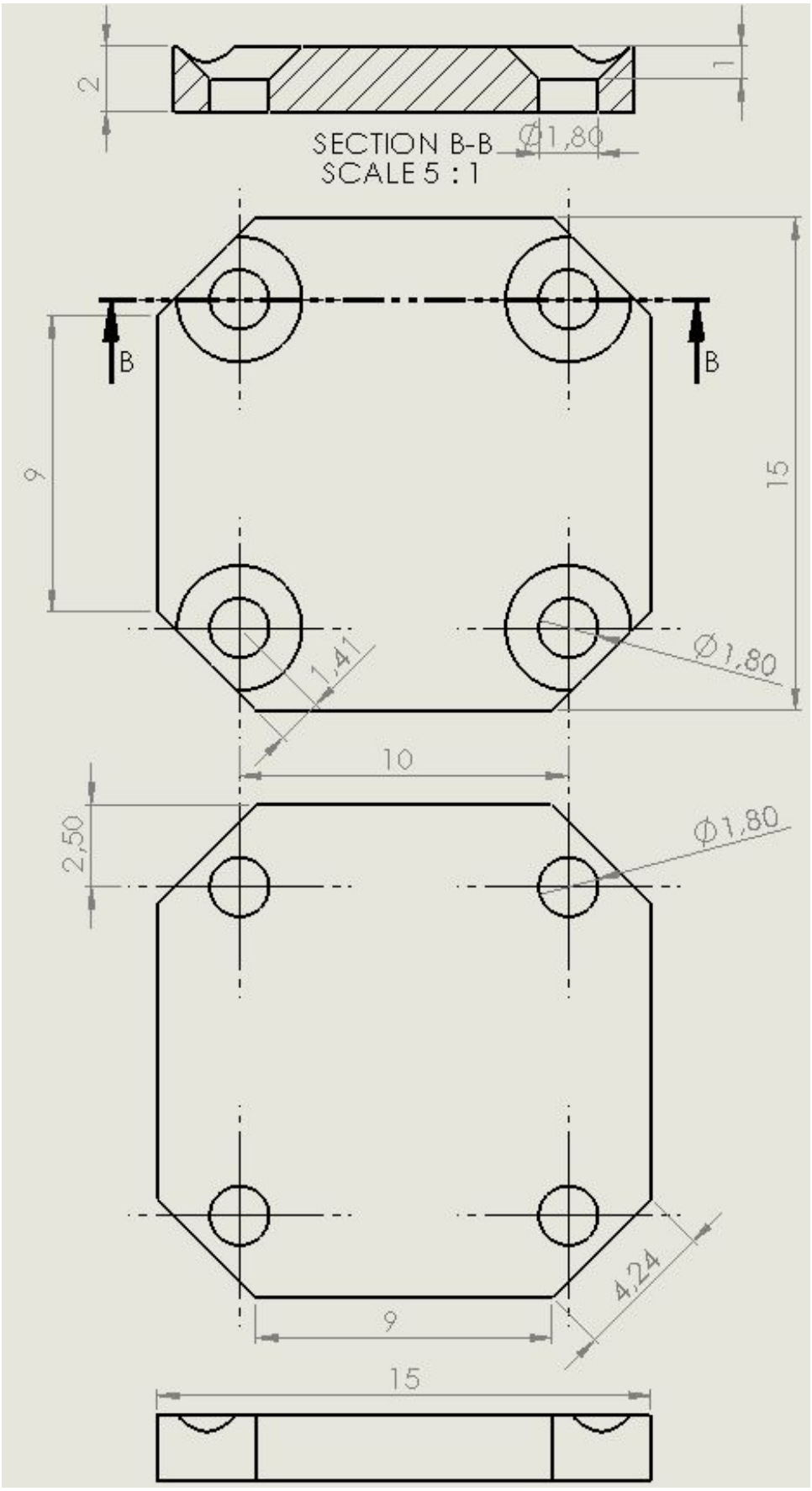

Figure 44: Solidworks model drawing of the prism mounting plate used in the inner frame of the cryostat holder

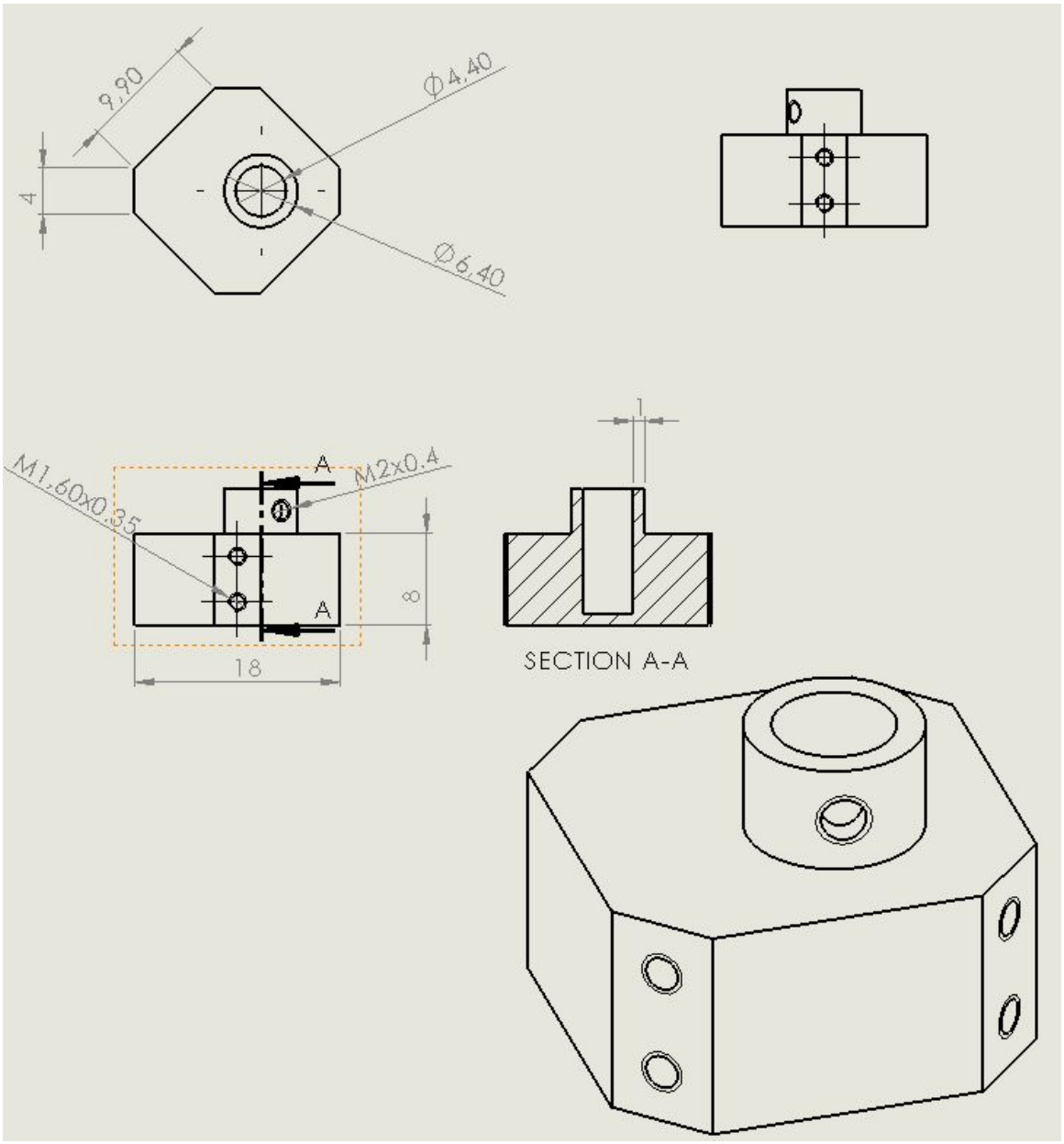

Figure 45: Solidworks model drawing of the Whispering Gallery Mode Resonator base plate used in the inner frame of the cryostat holder

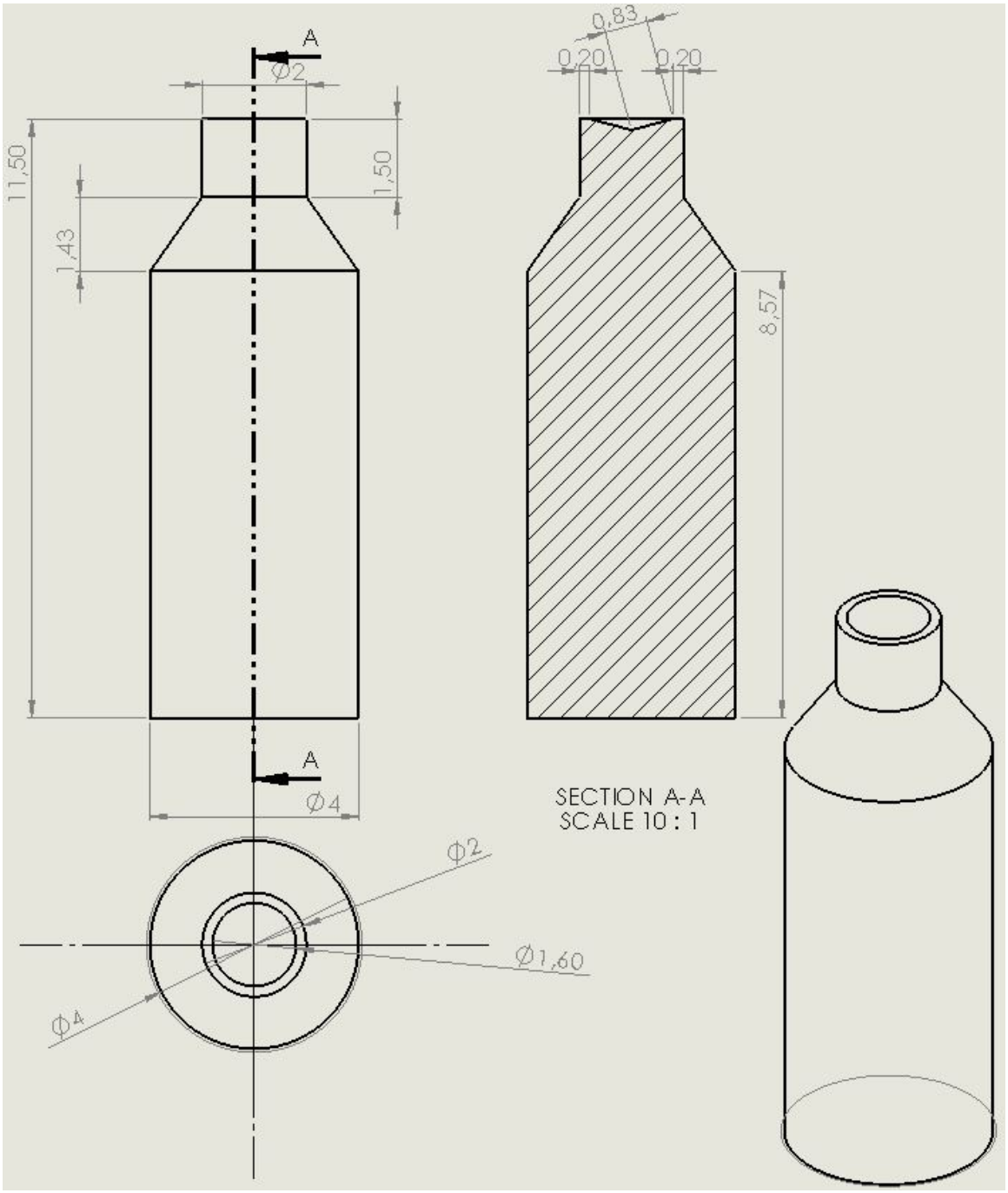

Figure 46: Solidworks model drawing of the Whispering Gallery Mode Resonator stand used in the inner frame of the cryostat holder

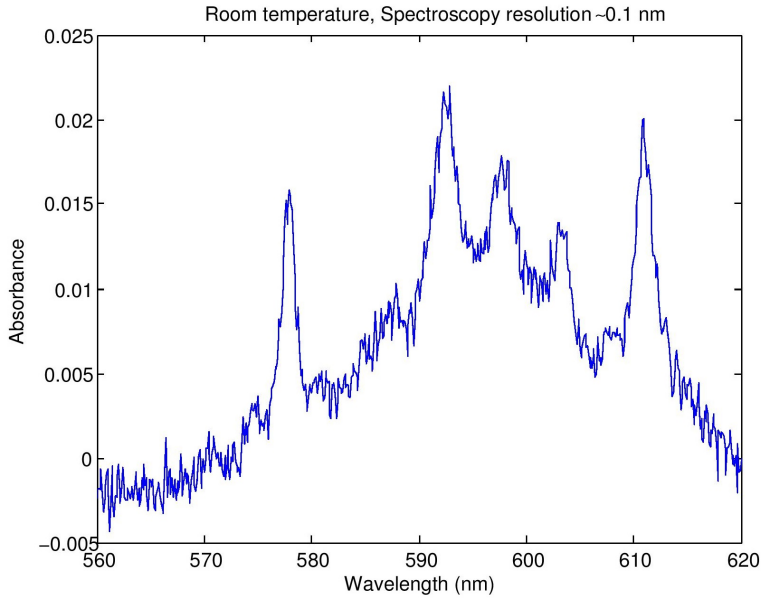

Figure 47: Absorbance spectrum of Praseodymium ions at room temperature, taken by Lund University Chemistry Department